Regional and clonal T cell dynamics at single cell resolution in immune checkpoint blockade

Joy A. Pai[1]*, Andrew Chow[2,3,4]*, Jennifer L. Sauter[5], Marissa Mattar[6], Hira Rizvi[7], Hyung Jun Woo[8], Nisargbhai Shah[3], Fathema Uddin[3], Alvaro Quintanal-Villalonga[3], Joseph M. Chan[3,4], Parvathy Manoj[3], Viola Allaj[3], Marina Baine[5], Jamie Chaft[3,4], Andrew J. Plodkowski[9], Helen Won[8], Daniel Wells[10], Mark T.A. Donoghue[8], Elisa de Stanchina[6], Triparna Sen[3,4], Jedd D. Wolchok[2,3,4,11,12], Brian Houck-Loomis[7], Taha Merghoub[2,3,4,11,12], Charles M. Rudin[3,4,7], Ansuman T. Satpathy[1]†, Matthew D. Hellmann[3,4,11]†

[1]Department of Pathology, Stanford University, Stanford, CA, USA
[2]Ludwig Collaborative and Swim Across America Laboratory, Memorial Sloan Kettering Cancer Center, New York, NY, USA.
[3]Department of Medicine, Memorial Sloan Kettering Cancer Center, New York, NY, USA.
[4]Weill Cornell Medical College, New York, NY, USA.
[5]Department of Pathology, Memorial Sloan Kettering Cancer Center, New York, NY, USA.
[6]Antitumor Assessment Core Facility, Memorial Sloan Kettering Cancer Center, New York, NY, USA.
[7]Druckenmiller Center For Lung Cancer Research, Memorial Sloan Kettering Cancer Center, New York, NY, USA.
[8]Marie-Josée and Henry R. Kravis Center for Molecular Oncology, Memorial Sloan Kettering Cancer Center, New York, NY, USA.
[9]Department of Radiology, Memorial Sloan Kettering Cancer Center, New York, NY, USA.
[10]Parker Institute for Cancer Immunotherapy, San Francisco, CA, USA; Immunai Inc., New York, NY, USA.
[11]Parker Institute for Cancer Immunotherapy, Memorial Sloan Kettering Cancer Center, New York, NY, USA.
[12]Human Oncology and Pathogenesis Program, Memorial Sloan Kettering Cancer Center, New York, NY, USA.
*These authors contributed equally to this manuscript.
†These authors contributed equally to this manuscript.
Correspondence to: satpathy@stanford.edu and hellmanm@mskcc.org

56   **ABSTRACT**

57   Paired T cell receptor and RNA single cell sequencing (scTCR/RNA-seq) has allowed for enhanced
58   resolution of clonal T cell dynamics in cancer. Here, we report a scTCR/RNA-seq dataset of 162,062 single
59   T cells from 31 tissue regions, including tumor, adjacent normal tissues, and lymph nodes (LN), from three
60   patients who underwent resections for progressing lung cancers after immune checkpoint blockade (ICB).
61   We found marked regional heterogeneity in tumor persistence that was associated with heterogeneity in
62   CD4 and CD8 T cell phenotypes; regions with persistent cancer cells were enriched for follicular helper
63   CD4 T cells (TFH), regulatory T cells (Treg), and exhausted CD8 T cells. Clonal analysis demonstrated that
64   highly-expanded T cell clones were predominantly of the CD8 subtype, were ubiquitously present across
65   all sampled regions, found in the peripheral circulation, and expressed gene signatures of 'large' and 'dual-
66   expanded' clones that have been predictive of response to ICB. Longitudinal tracking of CD8 T cell clones
67   in the peripheral blood revealed that the persistence of ubiquitous CD8 T cell clones, as well as
68   phenotypically distinct clones with tumor-reactive features, correlated with systemic tumor control. Finally,
69   tracking CD8 T cell clones across tissues revealed the presence of TCF-1$^+$ precursor exhausted CD8 T
70   cells in tumor draining LNs that were clonally linked to expanded exhausted CD8 T cells in tumors.
71   Altogether, this comprehensive scTCR/RNA-seq dataset with regional, longitudinal, and clonal resolution
72   provides fundamental insights into the tissue distribution, persistence, and differentiation trajectories of ICB-
73   responsive T cells that underlie clinical responses to ICB.

74
75
76
77
78
79
80
81
82
83
84
85
86
87
88
89
90
91
92
93
94
95
96
97
98
99
100
101
102
103
104
105
106
107
108
109
110
111

INTRODUCTION

Immune checkpoint blockade (ICB) has been a remarkable clinical advance in the treatment of cancer. Nonetheless, the majority of patients do not benefit from ICB therapy, and many of those who do eventually succumb to the disease. Emerging data has highlighted that ICB operates in cancer by unleashing a systemic CD8 response[1,2]. Unfortunately, isolated tumor biopsies at the time of resistance to ICB are limited in their ability to capture T cell dynamics at a systemic level since resistance can manifest heterogeneously across sites[3]. Moreover, although multiregional analyses have revealed substantial immune heterogeneity within an individual tumor lesion in early-stage lung cancer[4,5], it is unknown whether intra-lesional heterogeneity occurs in the metastatic setting where ICB is most often deployed.

More generally, compared to murine model systems, deconvolution of T cell responses to cancer in humans has been limited by the infeasibility of multi-region and longitudinal profiling of clonally related T cells. The development of paired scTCR/RNA-seq has enabled the deep profiling of T cells in the context of their TCR clonality, phenotypic heterogeneity, tissue distribution, and peripheral persistence[6]. However, few existing datasets have sufficient breadth to allow characterization of T cell clonal dynamics across anatomic sites and over time in the peripheral blood of individual patients. For example, while TCF-1^{+} precursor exhausted T cells have been elegantly profiled in murine systems[7] and T cells with the phenotype of TCF-1^{+} precursor exhausted cells were recently described in human LNs[8], evidence for the existence of a TCF-1^{+} precursor exhausted LN-resident CD8 T cell that is clonally linked to its exhausted counterpart in the tumor tissue is lacking. Relatedly, while T cell persistence is an established concept in the field of adoptive T cell therapies[9,10], a substantial barrier to our understanding of resistance to ICB therapy is knowing which T cell clones are the functionally important ones to track.

To help address these gaps, we performed paired scTCR/RNA-seq from 32 tumor, adjacent normal tissue, and regional LNs from four surgical resections from three patients undergoing ICB and profile regional T cell heterogeneity that is associated with pathologic tumor heterogeneity. From this T cell dataset, we were able to assess whether T cell paradigms previously demonstrated in mouse models could also be extended to human disease. Specifically, we identified TCF-1^{+} precursor exhausted cells in the LN of patients that are clonally related to exhausted CD8^{+} T cells in lung tumors. Furthermore, with deep profiling of cell states in the tissues, we were able to select clonal T cells to track in the peripheral blood over time during the course of ICB in three patients, leading to the observation that rapid disease progression was associated with a loss of persistence of both tumor-reactive and ubiquitous clones, suggesting that a broad array of T cells may contribute to the ongoing efficacy of ICB therapy.

RESULTS

Clinical and pathological characteristics of lung cancer resections after ICB

We profiled three patients (MSK 1263, 1302, and 1344) with metastatic non-small cell lung cancer (NSCLC) who were treated with anti-PD-1 monotherapy at Memorial Sloan Kettering Cancer Center (**Table S1**). All three patients had mixed responses, with most metastatic sites demonstrating clear response but at least one site showing progression or persistence during treatment (**Fig 1A**). In these cases, the evidently resistant site of disease was surgically resected, and multiple regions from each metastasis were collected for analyses. Following resection, two patients (MSK 1302 and 1344) remain alive nearly two years afterwards, while one patient (MSK 1263) quickly developed systemic disease recurrence and died.

From the three patients, we obtained four tumor resection specimens that underwent sectioning into eight 1-2cm^2 sections per primary tumor that were subjected to pathological evaluation, regional bulk RNA sequencing, flow cytometry, and scTCR/RNA-seq of sorted CD3^{+} T cells (**Fig 1B**). We also obtained adjacent normal tissue and regional LNs (not involved by tumor on pathological analysis) from MSK 1263 and 1302. Serial peripheral blood samples were collected up to 216, 452, and 1013 days after the start of anti-PD-1 therapy in MSK 1263, 1302, and 1344, respectively, to permit clonal tracking of peripheral T cells before, at, and after resection.

Pathological analysis revealed substantial tumor heterogeneity among the various tissue regions (**Fig S1**, **Table S2**). MSK 1263 and 1302 each had four regions involved by varying amounts of cancer cells and four regions not involved by viable cancer cells (**Fig S1A-B**); MSK 1344 had viable cancer cells in all regions but with varying involvement (**Fig S1C**). Bulk RNA sequencing of tumor regions also demonstrated inter-regional heterogeneity, particularly in MSK 1263 and 1302 (**Fig S2A**). Using CIBERSORT deconvolution, we noted that the two patients with greater pathological heterogeneity (MSK 1263 and 1302) also had greater regional heterogeneity for estimated immune cell frequencies (**Fig S2B**). To compare gene expression profiles between tumor regions with and without viable cancer cells, we performed gene set

168 enrichment analysis (GSEA) and found that pathways associated with cell cycle such as 'G2M checkpoint',
169 'DNA repair', and 'mitotic spindle' and also cancer aggressiveness such as 'epithelial mesenchymal
170 transition' and 'myc targets' were selectively upregulated in regions with viable cancer (**Fig S2C**, **Table S3**).
171 The tumor regions with viable cancer cells also showed enrichment for pathways that indicate an ongoing
172 immune response, such as 'inflammatory response' and 'interferon gamma response' (**Fig S2C**, **Table S3**).
173 These results suggest that immune cell state differences may be a critical driver of the pathologic
174 heterogeneity. Since intra- and inter-patient heterogeneity can be obscured by bulk analysis, we
175 hypothesized that applying scTCR/RNA-seq to CD3+ T cells (**Fig S2D**) – the critical effectors in ICB – in
176 these heterogeneous regions could yield important insights into the systemic anti-tumor T cell response
177 during ICB.
178
179 **Single cell TCR/RNA sequencing reveals inter- and intra-patient heterogeneity**
180 From the 32 adjacent normal, tumor, and LN regions, we performed droplet-based scTCR/RNA-
181 seq on sorted CD3+ T cells. 31 of 32 regional samples passed initial quality control assessment based on
182 mitochondrial content and the number of genes and UMIs detected per cell (**Fig S3A**, **Table S2**). After
183 removing the single region that did not pass QC, 63.5-89.9% of the individual cells per region (**Fig S3B**,
184 **Table S2**) passed QC filtering, retaining 162,062 high-quality T cells for downstream analyses. At least one
185 chain of the TCR was captured in 141,110 cells (87% of the cells that passed QC, 76.0-92.7% per region,
186 **Fig S3C**, **Table S2**), and paired TCRαβ chains were captured in 103,181 cells in total. Utilizing Seurat
187 v3.1.4[11], T lymphocytes were clustered into six CD4 T, seven CD8 T, and one mucosal-associated invariant
188 T (MAIT) cell clusters (**Fig 1C**). These clusters were annotated by examining differentially expressed cluster
189 markers and comparing to previously published cluster definitions in other scRNA-seq datasets[12-14] (**Fig
190 1D**, **Fig S3D**, **Table S4**). Naïve CD4 T cells expressed *CCR7*, *SELL*, *IL7R*, and *LEF1*. Among the two CD4
191 T effector clusters found, CD4-EFF1 highly expressed *IL7R* and *CD69,* while CD4-EFF2 highly expressed
192 *GZMA*, *PRDM1*, and *CXCR6*. Two TFH clusters were annotated with CD4-TFH1 highly expressing *ICOS*,
193 *TNFRSF4*, *TNFRSF18*, *CTLA4*, *SELL*, *TIGIT*, and *PRDM1,* and CD4-TFH2 highly expressing *ICOS*,
194 *PDCD1*, and *CXCL13*. CD4 Tregs highly expressed *FOXP3*, *TNFSFR9*, *TNFRSF18*, *TIGIT*, and *ENTPD1*.
195 Similar to naïve CD4 T cells, naïve CD8 T cells highly expressed *SELL, CCR7,* and *IL7R*. There were two
196 effector CD8 clusters: CD8-EFF highly expressed *GNLY*, *NKG7*, *PRF1*, and *KLRG1*, whereas CD8-GZMK
197 highly expressed *GZMK*, *CCL4*, *NKG7*, *GZMA*, *GZMH*, *PRF1*, *LAG3*, and *PDCD1*. A CD8 tissue resident
198 memory (TRM) cluster highly expressed *ITGAE*, *CD69*, *PDCD1*, *ZNF683*, *CXCR3*, *GZMA*, and *GZMB*. A
199 CD8 cluster that highly expressed *GMZK*, *LAG3*, *NKG7*, *ENTPD1*, *HAVCR2*, *CD38*, *CD274*, and *TCF7* was
200 annotated as CD8-TCF1. Finally, two exhausted CD8 T cells clusters that were distinguished by their
201 proliferative status were identified. CD8-EXH highly expressed *GZMB*, *LAG3*, *NKG7*, *ENTPD1*, *HAVCR2*,
202 *CXCL13*, *TNFRSF9,* and *IFNG,* while CD8-PROLIF-EXH expressed high levels of these genes in addition
203 to *GZMA*, *CD38*, and proliferation genes (*TUBB*, *TUBA1*, *MKI67*, *AURKB*). Importantly, all clusters were
204 represented across the four resections from the three patients (**Fig S4A-B**) and across region types (**Fig
205 S4C**).
206 We next utilized our scTCR-seq data to identify and link T cell clones to their cellular phenotypes.
207 As expected, there was minimal TCR overlap among the three patients (0 out of 45,607 unique CDR3αβ
208 nucleotide sequences, 2 sequences out of 45,538 unique CDR3αβ amino acid sequences, **Fig S4D**),
209 demonstrating that the rearranged TCR repertoire is specific to each patient and likely responding to
210 patient-specific antigens. By pairing TCR information with phenotypes, we observed that CD8 T cell clusters
211 contained clones with substantially larger clone sizes relative to CD4 T cell clusters (**Fig 1E**). We next
212 evaluated TCR repertoire similarity across the regions using the Morisita-Horn Index to globally evaluate
213 TCR heterogeneity in the three patients. Relative to MSK 1263 and 1302, 1344 has less heterogeneity of
214 represented T cell clones across the different regions (**Fig 1F**), perhaps concordant with this sample having
215 viable tumor throughout each region and being derived from a metastatic LN that may contribute greater
216 background homogeneity of non-tumor-associated T cells. Furthermore, the TCR composition within the
217 three sequenced adrenal regions from MSK 1263 were more similar to each other than to the primary tumor
218 or adjacent normal regions (**Fig 1F**). These data suggest that integration of TCR repertoire overlap across
219 regions with cell state and pathological features will yield informative insights into the clonal T cell
220 architecture during ICB.
221
222 **Treg, TFH, and exhausted CD8 T cells are enriched in tumor regions with viable cancer cells**

223   We next evaluated whether specific T cell phenotypes were enriched in regions containing viable
224   tumor cells (**Fig S4C**). We focused on 20 thoracic regions from MSK 1263 and 1302 resection samples that
225   included all representative region types (i.e. LN, adjacent normal, regions without viable tumor cells, and
226   regions with viable tumor cells). In contrast, the adrenal resection from MSK 1263 and LN resection from
227   MSK 1344 did not contain tumor bed regions without viable cancer, and thus, were not included in this
228   analysis. Among CD4 T cell clusters, we observed that CD4-Naïve, CD4-TFH1, and CD4-TFH2 cells were
229   enriched in LNs, and CD4-EFF2 was enriched in adjacent normal regions (**Fig 2A**). CD4-TFH1, CD4-TFH2,
230   and CD4-TREG cells were enriched in tumor regions relative to adjacent normal regions, and these cells
231   were further enriched in viable tumor regions relative to the regions of the tumor bed without viable tumor.
232   These three CD4 clusters also displayed higher Gini indices among TCR clones in the viable tumor regions,
233   indicating higher levels of clonal expansion (**Fig S5A**). Furthermore, by using TCRαβ sequences to trace T
234   cell clones across regions, we observed that clones enriched among regions with viable tumor were over-
235   represented by TFH phenotypic clusters (**Fig S5B-C**). Among CD8 T cell clusters, we observed that LNs
236   were enriched for CD8-Naïve and CD8-TCF1 cells, while adjacent normal regions were enriched in CD8-
237   EFF cells (**Fig 2B**). The two exhausted CD8 clusters were enriched in the tumor regions relative to adjacent
238   normal regions, and this effect was more pronounced in the tumor bed regions with viable cancer cells,
239   which is consistent with prior reports[12,15,16]. These exhausted CD8 clusters also demonstrated greater clonal
240   expansion relative to the adjacent normal and tumor regions without viable cancer cells (**Fig S5D**). These
241   findings are consistent with prior reports of clonal T cell expansion in tumor regions in human lung cancer[17].
242   Next, we characterized cell state differences between CD8 T cells across the regions by scoring
243   each cell in terms of a T cell exhaustion signature[18] (**Table S5**), which revealed that viable tumor areas
244   displayed the highest level of exhaustion (**Fig 2C**). To verify this finding, we performed flow cytometry on
245   CD8 T cells and found that cells from viable tumor regions expressed higher levels of the exhaustion
246   markers CD39 and PD-1 than cells from other regions (**Fig 2D-E**). We next sought to leverage the TCR
247   'barcode' to determine whether clonal T cells present in both non-viable and viable tumor regions
248   demonstrated greater exhaustion in proximity to viable cancer cells. In this clone-matched analysis of 851
249   CD8 clones (612 from MSK 1263; 239 from MSK 1302), CD8 T cells demonstrated a greater exhaustion
250   score in viable tumor regions than in non-viable tumor regions (**Fig 2F**), suggesting that cells within a clone
251   can take on distinct cell states depending on positioning within the tumor. In the two regions from the adrenal
252   resection from MSK 1263, there was also a positive correlation on flow cytometry between presence of
253   viable cancer cells and level of CD39 and PD-1 expressed (**Fig 2G**). Finally, we hypothesized that T cell
254   states that are concomitantly present in the same region may cross-signal to influence anti-tumor activity.
255   To assess for such interactions, we assessed spatial correlations of T cell states. Across the three patients,
256   we noted a strong correlation between the frequencies per region of CD4-TFH1, CD4-TFH2, CD4-TREG,
257   CD8-EXH, and CD8-PROLIF-EXH (**Fig 2H**), which are the cell subsets enriched in regions with viable
258   cancer cells (**Fig 2A-B**). In summary, T cells within regions with viable tumor adopt a more exhausted-like
259   state, even in comparison to their clonal counterparts within regions without viable tumor.
260
261   **Clonal expansion of tumor regional T cells is not associated with cancer cell-induced proliferation**
262   We next sought to better understand T cell heterogeneity based on the regional patterns of TCR
263   clone presence. Large clone sizes could be driven by the local expansion in tumor regions or be explained
264   by a larger precursor frequency. To distinguish these two possibilities, we asked whether clonal frequency
265   correlates with the number of regions in which the TCR clone was found. Indeed, there was a strong
266   correlation between overall clone frequency in the scTCR/RNA-seq dataset and the number of regions in
267   which the clone was found (**Fig S6A**), suggesting that large clone sizes are not exclusively driven by local
268   expansion. We next categorized TCRs into mutually exclusive regional patterns for each patient (**Fig S6B-
269   C**, Methods). 'Ubiquitous' TCRs were defined as those found in all LN, adjacent normal, and tumor regions
270   sampled, whereas 'LN enriched' and 'normal enriched' clones were those not found in tumor regions, but
271   found in LN and adjacent normal regions, respectively. 'Tumor enriched' clones were those found only in
272   tumor regions, but not LN and adjacent normal regions. These 'tumor enriched' clones were further sub-
273   classified as 'single region', 'oligo-regional', or 'pan-regional' if they were observed in only one, multiple but
274   not all, or all tumor regions, respectively. Clones with the 'Tumor enriched' profile, preferentially found in
275   regions of viable tumor (**Fig 3A**), might represent selective amplification by cancer cell-mediated clonal
276   expansion. Considering the clonal expansion of TFH, Treg, and exhausted CD8 T cells in viable tumor
277   regions, we hypothesized that tumor antigen-specific TCR-driven proliferation in the tumor
278   microenvironment mediated this enrichment. Indeed, others have proposed that CD8 T cells undergo an

279   additional burst of proliferation in the vicinity of viable tumor, potentially attributable to re-engagement of
280   the TCR in the tumor microenvironment[16]. By identifying TCR clones present in both the tumor regions with
281   and without viable cancer cells, we examined the proliferation of clone-matched T cells in the two regions.
282   Surprisingly, we did not find transcriptional evidence for enhanced proliferation of clone-matched T cells
283   residing in the Treg, TFH, or exhausted CD8 clusters within viable tumor regions (**Fig 3B-D**). These data
284   suggest that local tumor-induced proliferation of T cells is not the primary mechanism of clonal T cell
285   expansion in the tumor microenvironment.
286   We next evaluated preferential chemotaxis into regions with viable tumor cells, since enhanced
287   proliferation could not account for the accumulation of TFH, Treg, and exhausted CD8 T cells in the tumor
288   microenvironment. Relative to tumor bed regions without viable cancer cells, the regions with viable tumor
289   cells displayed higher bulk transcriptional expression of *Cxcl9, Cxcl10, and Cxcl16* (**Fig 3E**, **Fig S7A**). Thus,
290   we queried for expression of their corresponding chemokine receptors, *Cxcr3 and Cxcr6,* among the T cell
291   subsets in our scRNA-seq dataset. We observed that *Cxcr3 and Cxcr6* were the only chemokine receptors
292   preferentially expressed in Treg and exhausted CD8 T cells (**Fig 3F**, **Fig S7B**). Thus, chemotaxis of
293   CXCR3/CXCR6+ clonally expanded TFH, Treg, and exhausted CD8 T cells towards CXCL9, CXCL10, and
294   CXCL16, which are abundant in tumor bed regions with viable cancer cells, may explain their accumulation
295   in these areas. Finally, another explanation for the enrichment of TFH, Treg, and exhausted CD8 T cells in
296   the regions with viable tumor cells is increased survival potential of chronically stimulated T cells. Indeed,
297   we observed that the mitochondrial reads were consistently lower (except among Treg) among clone-
298   matched T cells in the viable tumor region (**Fig 3G-I**), suggesting that T cells in the tumor microenvironment
299   have activated mechanisms to promote survival in the setting of chronic antigen stimulation. The correlation
300   of enhanced exhaustion with reduced cell death in the viable tumor regions (**Fig 2C, Fig 3G-I**) is consistent
301   with the concept that the exhaustion program protects T cells from chronic antigen overstimulation that can
302   result in loss of CD8 T cell persistence[19].

Loss of ubiquitous clones is associated with rapid progression during ICB
305   Having characterized regional T cell clones, we next sought to investigate the nature of TCR clones
306   present across all regions, including adjacent normal tissue and the LN. As expected, ubiquitous clones
307   had the highest proportion of clones that could be observed in clone sizes over 50 and were composed
308   largely of T cells from the effector CD8 clusters (**Fig S6D-G**). Ubiquitous clones scored highly for the
309   previously reported signatures of 'large clones' and 'dual expanded' clones, which were both associated
310   with the success of ICB[14,20] (**Fig 4A-B**, **Table S5**), and were over-represented among the clones enriched
311   in regions with no viable tumor (**Fig 3A**). The ubiquitous clones did not preferentially display tumor-specific,
312   nor virus-specific, signatures (**Fig S6H-K**). To examine whether these ubiquitous clones were present in
313   the circulation as well, we performed bulk TCRβ sequencing from the peripheral blood of our cohort of three
314   patients at multiple time points after ICB, which included the time period before, during, and after resection.
315   The latest blood collection ranged from 216 to 1013 days after the start of ICB (**Table S1**). Along with their
316   widespread presence across regions, ubiquitous clones were also observed more frequently in the
317   peripheral blood relative to clones with other regional patterns, which supports the systemic presence and
318   replenishment of these clones (**Fig 4C-D**). Next, we utilized the bulk TCRβ sequencing data to compare
319   the peripheral persistence of ubiquitous clones throughout the course of ICB therapy in the three patients.
320   Despite the relative stability of T cell clones categorized into the non-ubiquitous groups (**Fig S8**), there was
321   a substantial reduction in the peripheral persistence of ubiquitous T cell clones in MSK 1263, but not MSK
322   1302 and 1344 (**Fig 4E**). Thus, rapid disease progression was associated with a loss of persistence of
323   ubiquitous clones in MSK 1263, suggesting that these ubiquitous T cells may contribute to, or reflect, the
324   immune response that is critical for the ongoing efficacy of ICB therapy.

CD8 T cell clones with tumor-reactive features can be tracked in the blood and correlate with systemic efficacy of ICB
328   From our longitudinal analysis of peripheral blood in our cohort, we next assessed whether the
329   different T cell clusters in resected tumors were differentially represented in the peripheral blood. For both
330   CD4 and CD8 T cell clusters, we noted substantial heterogeneity in the representation of the various
331   clusters in the peripheral blood, both when the circulating TCR clone was linked to each T cell state found
332   in the tissues (**Fig 5A**) and when linked to its majority phenotype in the tissue (**Fig S9A**). Among CD4 T
333   cells, Treg clones in the tissue were the least prevalent, while CD4 effector T clones were the most prevalent
334   in the peripheral blood (**Fig 5A**, **Fig S9A**). Among CD8 T cells, the variability was even more striking: TCR

335   clones associated with the CD8-TCF1 cluster were the least prevalent in the peripheral blood, whereas
336   clones associated with the CD8-EFF cluster were the most prevalent, with an almost 1000-fold difference
337   between the two (**Fig 5A**). We next assessed the peripheral persistence of clones linked to the various
338   tissue-defined T cell clusters. CD4 and MAIT clusters were largely stable throughout each patient's time on
339   ICB therapy (**Fig 5B-C**, **Fig S9B**). Notably, T cell clones of the CD8-EFF phenotype, which was
340   overrepresented among clones enriched in non-viable tumor regions (**Fig S5C**), increased at the time of
341   resection for both MSK 1263 and 1344 (**Fig 5B-C)**. In contrast, there were patient-specific patterns in the
342   peripheral dynamics of CD8 T cell clones linked to other cell states in tissue. For example, MSK 1302 and
343   1344 had peripheral stability and persistence of TCR clones linked to CD8 tissue clusters, while MSK 1263
344   (the only patient to progress quickly after resection) showed cluster-specific changes (**Fig 5B-C**, **Fig S9B**).
345   Unlike the stability of naïve CD8 T cell clones, clones associated with CD8-GZMK, CD8-TRM, CD8-
346   PROLIF-EXH, and CD8-EXH steeply declined in the peripheral blood at the time of oligometastatic
347   resection (second timepoint). Additionally, while CD8-TCF1 T cell clones were stable at the time of the first
348   oligometastatic resection, there was a substantial decline at the time of the second oligometastatic adrenal
349   resection (**Fig 5B**). Taken together, these results suggest that loss of peripheral persistence of CD8 clones
350   with exhausted T cell states coincides with disease progression.
351   Persistence of adoptively transferred T cells is strongly correlated with their durable clinical
352   activity[9,21]. Due to the logistical difficulty of tracking a multitude of tumor-reactive CD8 T cell clones, the
353   importance of persistence of endogenous tumor-reactive T cell clones is not well established. To hone in
354   on the CD8 T cells that are more likely to exert direct cytotoxicity against the cancer, we derived a tumor-
355   reactivity signature score based on published features of tumor-reactive CD8 T cells[22] (**Table S5**).
356   Consistent with prior reports that exhausted T cells comprise the tumor-reactive population[22-28], we found
357   that the exhausted CD8 T cell clusters had the highest tumor-reactivity score (**Fig 6A**, **Table S5**). Two
358   recent publications reported empirically validated transcriptional features of tumor- vs. virus-specific CD8 T
359   cells in human lung cancer and melanoma[27,28] (**Table S5**). Concordantly, CD8 T cells in our dataset with
360   tumor-reactivity scores >0 (TR^{hi}) had a greater signature score for tumor specificity from these datasets
361   (**Fig 6B-C**), supporting the validity of the tumor-reactivity signature. Consistent with the enrichment of
362   exhausted CD8 T cells in the viable tumor regions, we observed that the CD8 T cells in the viable tumor
363   regions had the highest tumor-reactivity score (**Fig 6D**). Additionally, among the top 40 most expanded TR^{hi}
364   CD8 T cell clones (**Fig S10A**), clones were preferentially found in viable tumor regions, whereas TR^{lo} CD8
365   T cell clones were more enriched in the LN, adjacent normal lung, and tumor regions without viable cancer
366   (**Fig 6E**, **Fig S10B**). Furthermore, TR^{hi} CD8 T cell clones were often found in the exhausted T cell clusters,
367   CD8-TRM, and CD8-GZMK, whereas TR^{lo} CD8 clones were enriched in effector CD8 clusters (**Fig 6F**, **Fig
368   S10C**), suggesting that T cell clones with tumor-reactive features are preferentially present in an exhausted
369   state within regions with viable cancer.
370   To better understand potential differences in the cell state transitions among TR^{hi} vs. TR^{lo} CD8
371   clones, we performed pseudotime trajectory analysis on cells from the most highly expanded clones (**Fig
372   S10D-F**). We observed that the branches involving TR^{lo} clones occupy a distinct portion of the UMAP, which
373   is predominantly composed of CD8-EFF and CD8-GZMK phenotypes (**Fig S10F**). Since the branches
374   involving TR^{hi} clones also passed through the CD8-GZMK state, we asked whether there were any
375   differences between CD8-GZMK cells within TR^{hi} CD8 clones and those within TR^{lo} clones. Differential
376   gene expression analysis of cells in the CD8-GZMK cluster revealed an upregulation of *CCL5, GZMB,*
377   *GNLY, KLRB1*, and the exhaustion-related genes *HAVCR2, CTLA4, CXCL13* among TR^{hi} clones (**Fig 6G**).
378   In contrast, CD8-GZMK cells from TR^{lo} CD8 clones expressed higher levels of *GZMK*, *KLRG1*, *IL7R*, and
379   members of the AP-1 transcription factor family, including *FOS, FOSB, and JUNB*. These results suggest
380   that even within in the CD8-GZMK cluster, T cell clones exist in distinct cell states depending on reactivity
381   and interactions with the tumor.
382   Finally, we hypothesized that the peripheral persistence of TR^{hi} CD8 T cell clones might correlate
383   with systemic benefit from ICB. To evaluate this, we assessed the peripheral dynamics of TR^{hi} CD8 T cell
384   clones from the resected specimens. We observed a reduction in TR^{hi} T cell clones in MSK 1263 at the
385   time of the first resection, but not in MSK 1302 and 1344 (**Fig 6H**, **Fig S10G**). In fact, we were able to track
386   these clones in MSK 1344 for nearly three years after the start of ICB. Thus, MSK 1263, whose clinical
387   course was distinctly characterized by the shortened duration of benefit from ICB and rapid progression
388   following resection of disease, was uniquely found to have a marked reduction in CD8 T cell clones with
389   tumor-reactive features, suggesting that loss of persistence of these clones may contribute to immune
390   escape.

Intratumoral exhausted CD8 T cells can be found in a TCF-1^{+} progenitor state in the LN

Recent studies using TCR transgenic systems have demonstrated that exhausted CD8 T cells in the tumor derive from LN TCF-1^{+} precursor exhausted CD8 T cells[29-31] and that TCF-1^{+} populations can be found in human primary lung cancers[16] and LNs[8]. However, whether these TCF-1^{+} precursor exhausted cells originate from regional LNs in human cancers has not been demonstrated. To probe for a clonal relationship between TCF-1^{+} precursors and exhausted CD8 T cells, we first examined the CD8-TCF1 cluster. Compared to naïve CD8 T cells which can also express TCF-1, the CD8-TCF1 cluster preferentially expressed *SLAMF6, NKG7, CD38, CTLA4, HAVCR2, GZMA*, and *GZMK* (**Fig S11A-B**). Among 361 TCRαβ clones found in the CD8-TCF1 cluster, 36 could be found in other CD8 T cell clusters, including 15 in CD8-PROLIF-EXH and 4 in CD8-EXH (**Fig 7A-B**). As a parallel method to identify clonally-related TCF-1^{+} precursors, we surveyed CD8 TCRαβ clones that could be found in the exhausted CD8 state (CD8-EXH or CD8-PROLIF-EXH) in the tumor tissue of MSK 1263 and 1302 and identified clone-matched cells in the regional LN. We then assessed the percentage of the matched clones that had a *TCF7* transcript >0 (**Fig S11C**). We observed that 16.7% and 21.4% of intratumoral exhausted CD8 T cell clones with paired representation in the LN of MSK 1263 and 1302, respectively, were TCF-1^{+} (5.7% and 7.3% of total exhausted CD8 T cell clones, **Fig S11D**). Since TCF-1 expression may also mark naïve CD8 T cells rather than precursor exhausted populations, and since gene dropout might result in undercounting of TCF-1^{+} precursors, we repeated this analysis querying for a progenitor score (**Table S5**). With a cutoff of >0 for this progenitor score (**Fig S11E**), we noted that 24.3% and 35.7% of exhausted CD8 clones that could be found in the LN of MSK 1263 and 1302, respectively, could be found in a precursor exhausted state in the LN (8.4% and 12.2% of total exhausted CD8 T cell clones, **Fig 7C**). We also performed the same analysis using CD8 T cell clones that exhibited high exhaustion score among the tumor regions (**Fig S11F, Table S5**), which yielded a similar proportion of clones found in a LN progenitor state (**Fig 7D**, **Fig S11G**).

To assess how clonal CD8 T cell states vary across regions, we evaluated the frequency with which the progenitor phenotype of exhausted CD8 clones could be found in LNs, regions of no viable tumor, and regions of viable tumor from the thoracic regions of MSK 1263 and 1302. As expected, the progenitor score of CD8 T cells declined as these clonal CD8 T cells migrated from the LN to the tumor (**Fig 7E,G**). Comparing the profiles of the adrenal and thoracic lesions of MSK 1263, we observed that clones found in the thoracic or adrenal tumor regions similarly had a lower progenitor score compared to their clone-matched counterparts in the LN (**Fig 7F,H**). To characterize the human LN progenitor state from an unbiased perspective, we performed differential expression analysis of clone-matched CD8 T cells within the LN and tumor regions. As expected, we observed a higher level of *TCF7* in the LN (**Fig 7I**), as well as increased expression of *LEF1, SELL, GZMK,* and heat shock proteins (*HSPA1A, HSPA1B, HSPA6*). Conversely, cells within the tumor regions overexpressed *GZMB, GNLY*, and exhaustion-related markers such as *CXCL13* and *CTLA4*. Finally, to confirm these findings in another dataset, we examined scTCR/RNA-seq data from three patients with resection of primary tumor and regional LNs after receiving neoadjuvant nivolumab for lung cancer[27]. We observed that 12.8-21.6% of clone-matched CD8 T cell clones with high exhaustion scores could be observed in a TCF-1 state (**Fig 7J**, **Fig S11H**). In these patients, there was also a reduction in progenitor score when comparing clone-matched CD8 T cells between the LN and tumor (**Fig 7K**). Altogether, these data provide support for the existence of a TCF-1^{+} precursor exhausted T cell population in the LN that is clonally related to exhausted CD8 T cells in the tumor microenvironment.

DISCUSSION

Despite the characteristic durability of response to ICB, many patients with initial response will later develop acquired resistance[32]. Up to 65% of patients who initially obtained a radiographical response to anti-PD-1 therapy in lung cancer progressed within 4 months of follow up. As surgical resection is rarely performed as standard of care in metastatic lung cancer patients receiving ICB therapy, we believe that our dataset of four resected oligometastatic lesions provides a unique window into the regional heterogeneity of the ICB response. To our knowledge, this is the largest reported single cell dataset of human T cells with peripheral tracking of clones over time and serves as an important resource for the cancer immunology community. Insights from this dataset may help to inform strategies to overcome resistance to ICB.

In this study, we performed paired scRNA/TCR-seq of 162,062 T cells from 31 tissue regions, including matched tumor, adjacent normal tissues, and LNs from 3 patients. Using this dataset, we identified several insights into the tissue distribution, persistence, and differentiation trajectories of ICB-responsive T cells. First, we found substantial regional heterogeneity in tumor persistence that was associated with

447   cellular heterogeneity of both CD4 and CD8 T cell phenotypes. Specifically, we demonstrate that regions
448   with persistent cancer cells were enriched for CD4 TFH cells, Tregs, and exhausted CD8 T cells.
449   Furthermore, this phenotypic enrichment in viable tumor regions is associated with reduced T cell death,
450   rather than increased proliferation. Second, by investigating regional patterns of TCR clone presence, we
451   identify ubiquitous T cell clones that were present in all tissue compartments examined and bear similarity
452   to previously described 'large clones'[20] and 'dual expanded' CD8 clones[14] that have been associated with
453   benefit from ICB. Third, the general persistence of CD8 clones over time in the patients in this study is
454   consistent with other recent reports in lung cancer[17] and melanoma[28]. By incorporating recently reported
455   transcriptional profiles of empirically validated, tumor-specific CD8 T cells, we interrogated our dataset for
456   T cells with tumor-reactive features and profiled their persistence in the peripheral blood over the course of
457   treatment. We observed that a sharp reduction in CD8 T cell clones with TR[hi] and ubiquitous features was
458   associated with systemic progression of disease in MSK 1263, suggesting that a broad repertoire of T cell
459   clones may coordinately contribute to the ongoing efficacy of ICB. However, subsequent peripheral blood
460   tracking studies will be needed to further investigate the causal nature of this relationship. Finally, upon
461   interrogation of clone-matched T cells in the tumor and LN regions, we found definitive evidence of TCF-1^{+}
462   precursor exhausted CD8 T cells in the LN that are clonally related to terminally exhausted CD8 T cells
463   found in the tumor. Altogether, this work not only serves as a comprehensive single cell resource with
464   regional, longitudinal, and clonal resolution, but also provides insights into T cell responses that underlie
465   clinical responses to ICB.
466   A limitation of this current study includes the inability to simultaneously profile the tumor cells and
467   non-T immune cells from these patients as our focus was on T cell dynamics. Moreover, we were unable
468   to derive cell lines or patient-derived xenografts from these cases and thus, do not have viable material to
469   further interrogate the malignant cell compartment. Another limitation of the primary dataset is the limited
470   number of total patients represented. Moreover, since this study was not prospectively designed, there are
471   patient-specific differences in timing of tissue and blood collection. Future larger prospectively designed
472   studies will help to overcome these limitations.
473
474   **MATERIALS AND METHODS**
475   Human biospecimens
476   Resection materials and blood were obtained with informed consent from patients under protocol #06-107
477   approved by MSKCC.
478
479   Pathologic review
480   Histologic review for extent of tumor response was performed by J.L.S. following the IASLC
481   multidisciplinary recommendations for pathologic assessment of lung cancer resection specimens after
482   neoadjuvant therapy[33].
483
484   Bulk RNA-sequencing
485   Approximately 200-500 ng of FFPE RNA extracted from FFPE slides with a DV200 range between 3-99 or
486   65-100 ng of fresh frozen RNA (DV200 98-99) per sample were used for RNA library construction using the
487   KAPA RNA Hyper library prep kit (Roche, Switzerland). The number of pre-capture PCR cycles was
488   adjusted based on the quality and quantity of RNA extracted from the samples. Customized adapters with
489   3bp unique molecular indexes (UMI) (Integrated DNA Technologies, USA) and sample-specific dual-index
490   primers (Integrated DNA Technologies, USA) were added to each library. The quantity of libraries was
491   measured with Qubit (Thermo Fisher Scientific, USA) and the quality was assessed by TapeStation
492   Genomic DNA Assay (Agilent Technologies, US). Approximately 500 ng of each RNA library were pooled
493   for hybridization capture with IDT Whole Exome Panel V1 (Integrated DNA Technologies, US) using a
494   customized capture protocol modified from NimbleGen SeqCap Target Enrichment system (Roche,
495   Switzerland). The captured DNA libraries were then sequenced on an Illumina HiSeq4000 in paired ends
496   (2X100bp) to a target 50 million read pairs per sample. The demultiplexed FASTQs were aligned to the
497   human genome reference hg19/GRCh37 using STAR (v2.7.3a) and deduplicated from the combination of
498   UMI sequence and alignment coordinate using UMI-tools (v1.0.1). Rsubread (v2.6.4) was used to extract
499   the feature count matrix from alignments. We used edgeR (v3.34.1) for normalization, multidimensional
500   scaling, differential expression, and gene ontology (GO) enrichment analyses. For GSEA, we used fgsea
501   (v1.18.0) with MSigDB (v7.4) hallmark pathway gene set. Cell type deconvolution was performed using

502   CIBERSORTx (https://cibersortx.stanford.edu) with reference matrix derived from one lung tumor sample
503   (LUNG_T31) within previously published single-cell data[34].
504
505   Fresh tumor preparation
506   Gross resection specimens were promptly sectioned within 1 hour of the resection and tumor pieces from
507   the various regions were placed into human complete medium (RPMI + 10% human serum albumin + 1%
508   penicillin with streptomycin + 0.1% amphotericin) on ice. Human tissue from the various regions were
509   minced with a razor blade and digested in GentleMACS enzyme mix in individual tubes per region for 30-
510   60 minutes according to manufacturer's recommendations. After centrifugation of a filtered single cell mix,
511   the cell pellet was resuspended in human complete medium and underwent one round of ACK lysis. A
512   subset of this cell pellet was cryopreserved for future use in Bambanker media.
513
514   Flow cytometry and cell sorting
515   Cells were incubated with TruFCX (for human cells) to block nonspecific binding, and then stained (15 min,
516   4 °C) with appropriate dilutions of CD45-BV510 (clone 2D1), CD3-BV650 (clone UCHT1), CD8-PerCP-
517   Cy5.5 (clone SK1), CD4-Alexa700 (clone A161A1), CD39-APC (clone A1) , and PD-1-APC-Fire 750 (clone
518   EH12.2H7). All antibodies were purchased from BioLegend. DAPI$^-$ CD45$^+$ CD3$^+$ cells analyzed by a BD
519   LSRII or were sorted by FACS Aria. Doublets and dead cells were excluded on the basis of forward and
520   side scatter and 4′,6-diamidino-2-phenylindole (DAPI, 1μg/ml). Flow cytometry data was analyzed with
521   FlowJo V10.8 (TreeStar). Representative gating strategy is depicted in Fig S2D.
522
523   Single cell RNA sequencing
524   Sorted T cells were stained with Trypan blue and Countess II Automated Cell Counter (ThermoFisher) was
525   used to assess both cell number and viability. Following QC, the single cell suspension was loaded onto
526   Chromium Chip A (10X Genomics PN 230027) and GEM generation, cDNA synthesis, cDNA amplification,
527   and library preparation of 2,700-11,000 cells proceeded using the Chromium Single Cell 5' Reagent Kit
528   (10X Genomics PN 1000006) according to the manufacturer's protocol. cDNA amplification included 13-14
529   cycles and 11-50ng of the material was used to prepare sequencing libraries with 14-16 cycles of PCR.
530   Indexed libraries were pooled equimolar and sequenced on a NovaSeq 6000 or NextSeq 500 in a PE26/92,
531   PE28/91 or PE100 run using the NovaSeq 6000 SP, S1, or S2 Reagent Kit (100, 200, or 500 cycles) or TG
532   NextSeq 500/550 High Output Kit v2.5 (150 cycles) (Illumina). An average of 179 million reads was
533   generated per sample.
534
535   Single cell TCR sequencing
536   An aliquot of cDNA generated using the methods described above was used to enrich for V(D)J regions
537   using the Chromium Single Cell V(D)J Enrichment Kit Human T Cell (10X Genomics PN 1000005)
538   according to the manufacturer's protocol with 10 cycles of PCR during enrichment and 9 cycles during
539   library preparation. Indexed libraries were pooled equimolar and sequenced on a NovaSeq 6000 in a PE150
540   run using the NovaSeq 6000 SP, S1, or S4 Reagent Kit (300 cycles) (Illumina). An average of 129 million
541   paired reads was generated per sample.
542
543   Pre-processing of scTCR/RNA-seq libraries
544   Reads from 10x scRNA expression libraries were aligned to human genome assembly GRCh38 (hg19) and
545   quantified using cellranger count (10x Genomics, v3.1.0). The filtered feature-barcode matrices containing
546   only cellular barcodes were used for further analysis. Single cell gene expression matrices were imported
547   into R (v3.6.1) and analyzed using Seurat (v3.1.4)[11]. Cells with >4,500 genes captured and <15,000 UMIs
548   were kept. Additionally, cells with greater than 15% mitochondrial RNA reads were excluded from
549   subsequent analyses.
550
551   Single cell TCR reads were aligned to human genome assembly GRCh38 (hg19) and assembled into
552   reconstructed TCR consensus sequences using cellranger vdj (10x Genomics, v3.1.0). Only productive
553   TCRα and TCRβ sequences were considered for further analysis. Overall, TCR sequences were annotated
554   for 141,110 cells that passed RNA quality filtering, with paired TCRαβ sequences detected for 103,181
555   cells. Cells with multiple TCRβ chains captured (ββ, ααβ, ααββ) were excluded from further analysis. Only
556   cells with conventional paired TCR chain combinations αβ or ααβ were kept for downstream TCR clonal

557 analyses. Cells sharing the same CDR3αβ nucleotide sequences were defined as belonging to the same
558 TCR clone.
559
560 scRNA-seq data integration and clustering
561 scRNA-seq libraries from each region were log10-normalized individually and integrated with Seurat by
562 identifying anchors between datasets using reciprocal PCA with 30 dimensions. TCR genes were excluded
563 from the selection of integration anchors to prevent TCR chain driven biases. Dimensionality reduction of
564 the integrated matrix was performed using Uniform Manifold Approximation and Projection (UMAP) with
565 the first 30 principal components. Phenotypic clusters were defined by constructing a k-nearest neighbors
566 graph and identifying groups of cells using the Louvain algorithm with resolution of 0.6.
567
568 TCR clone regional pattern categorization
569 TCR clones were categorized into mutually exclusive regional patterns for each patient by assessing the
570 combination of region types (i.e. LN, adjacent normal, or tumor regions) for which cells with shared CDR3αβ
571 nucleotide sequences could be found in. 'Ubiquitous' TCR clones were defined as those found in all LN,
572 adjacent normal, and tumor regions sampled. 'LN enriched' and 'normal enriched' TCR clones were those
573 found only in LN or adjacent normal regions, respectively. 'Tumor enriched' clones were found only in tumor
574 regions, but not in LN nor adjacent normal regions, and were further sub-classified as 'single region' (found
575 in only one tumor region), 'oligo-regional' (found in >1 but not all tumor regions), or 'pan-regional' (found in
576 tumor regions).
577
578 TCR clone enrichment in viable/non-viable tumor
579 TCR clones were categorized as enriched in viable tumor regions or no viable tumor regions based on
580 CDR3αβ nucleotide sequence. For each clone, the number of cells found in viable tumor or no viable tumor
581 regions was calculated and constructed into a 2x2 contingency table to test for enrichment by Fisher's exact
582 test. Clones with p-value < 0.05 were considered enriched in viable or no viable tumor regions.
583
584 Gene signature scoring
585 To characterize cells according to previously reported gene signatures of tumor-reactivity, CD8 T cell
586 dysfunction, progenitor exhausted T cells, tumor- and viral-specificity, and expanded clones (**Table S5**),
587 gene scores were calculated per cell using the AddModuleScore function from Seurat.
588
589 Clone-matched analysis
590 To compare cell state differences between T cells in regions with no viable tumor vs. viable tumor, we
591 performed clone-matched analysis of Treg (CD4-TREG), TFH (CD4-TFH1 and CD4-TFH2), and exhausted
592 CD8 clones (CD8-PROLIF-EXH and CD8-EXH). For each phenotype, clones with at least one cell with the
593 given phenotype present in both no viable tumor and viable tumor regions were considered. Clonal scores
594 were calculated per region by averaging the scores of cells within each clone with the given phenotype in
595 each region.
596
597 To characterize T cell state transitions of CD8 clones between LN and tumor regions, CD8 clones in an
598 exhausted state were defined in two ways: (1) clones with tumor cells belonging to the CD8-EXH or CD8-
599 PROLIF-EXH phenotype cluster, or (2) clones displaying an average exhaustion score >0 among tumor
600 cells. Clonal progenitor scores were calculated per region by averaging the scores of cells within each clone
601 in each region.
602
603 Trajectory inference
604 To perform trajectory analysis of TR^{hi} vs. TR^{lo} CD8 T cell clones, dimensionality reduction of cells within the
605 top 40 most highly expanded TR^{hi} and TR^{lo} T cell clones was performed using UMAP as described above.
606 Pseudotime analysis was then performed with Monocle 3 (v0.2.1)[35] by learning a principal graph for the
607 data and ordering cells along the graph using the cells in the CD8-Naive phenotype cluster to select a root
608 node.
609
610 External scTCR/RNA-seq dataset analysis

611 Single cell data from Caushi et al[27] were obtained from GEO (GSE176021) and analyzed as described
612 above. Only samples from patients with matched LN and tumor samples (MD01-004, MD01-005, MD043-
613 011) were analyzed.
614
615 Bulk TCR sequencing
616 gDNA was extracted from the peripheral blood utilizing the AllPrep DNA/RNA Kit (Qiagen) and was sent to
617 Adaptive Biotechnologies for bulk TCRβ sequencing. Data was processed using the ImmunoSEQ Analyzer
618 (Adaptive Biotechnologies, v3.0).
619
620 Statistical analysis
621 Statistical analysis of bulk and single-cell sequencing data was performed in R (v3.6.1). Statistical analysis
622 of flow cytometry data was performed in GraphPad Prism (v9.0). All box and whisker plots are defined as:
623 center line, median; box, interquartile range; upper whisker limit, maximum without outliers; lower whisker
624 limit; minimum without outliers; points, outliers.

Figure 1
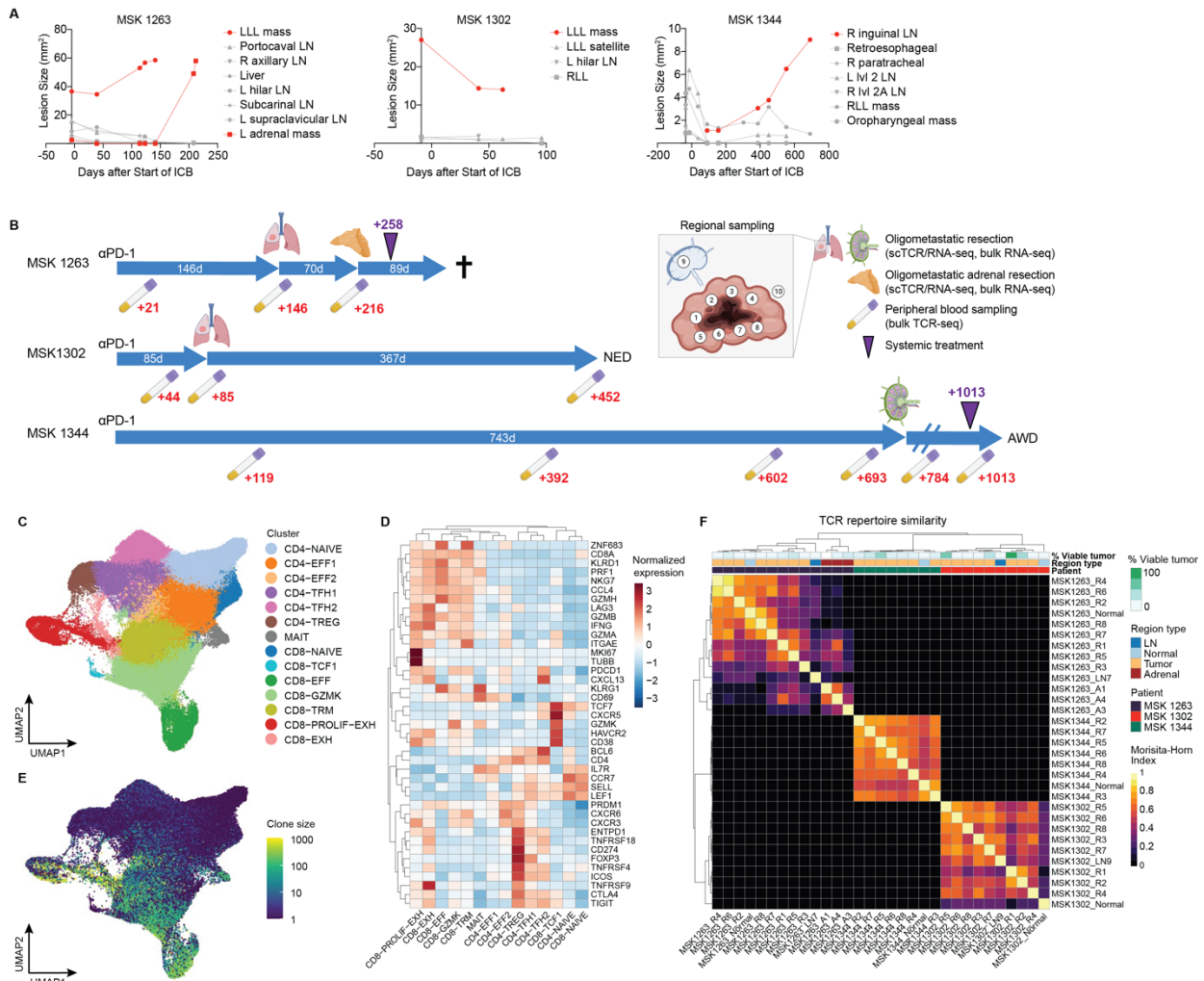
625
626 **Figure 1. Regional T cell heterogeneity in resections after ICB.**
627 A) Quantification of surface area of individuals lesions on radiographical studies over time in three patients.
628 Red lines indicate lesions that were resected and analyzed in this study.
629 B) Schematic of time interval from start of anti-PD-1 therapy to time of resections across the three patients.
630 Timeline of associated peripheral blood collections are indicated in red text below. Purple triangle indicates
631 a change in systemic therapy from anti-PD-1 monotherapy. Cross indicates patient death. NED = no
632 evidence of disease. AWD = alive with disease.
633 C) UMAP of cell clusters obtained from scTCR/RNA-seq of sorted CD3$^+$ T cells, which are further defined
634 in (D).
635 D) Heat map of differentially expressed genes found in each T cell cluster.
636 E) UMAP overlaid with TCRαβ clone size as assessed from scTCR-seq data.
637 F) Morisita-Horn Index of TCRαβ repertoire similarity among different regions (minimum clone size = 10).

Figure 2
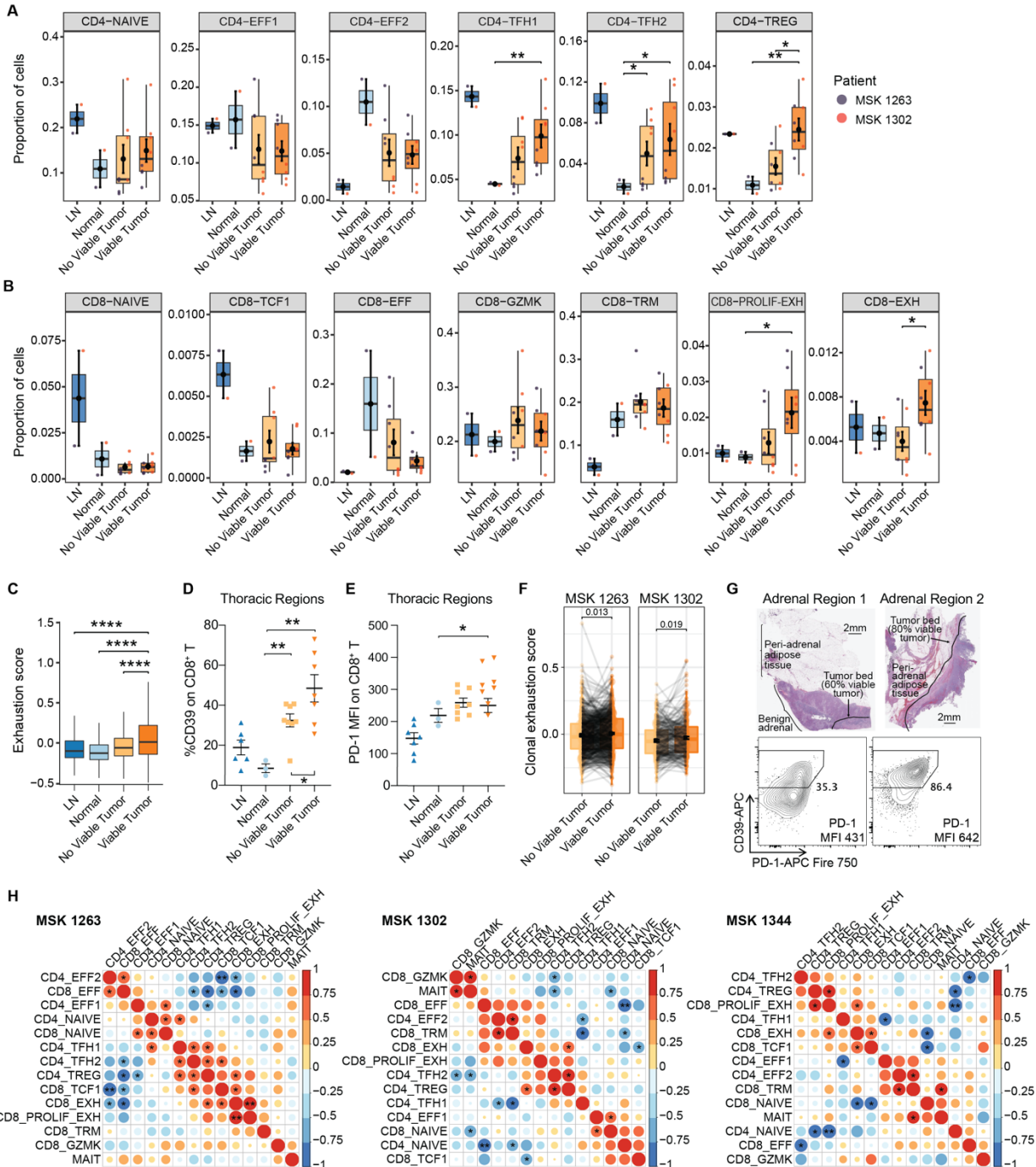
638
639 **Figure 2. Tumor regions with viable tumor are enriched in CD4 TFH, Treg, and exhausted CD8 T**
640 **cells.**
641 A) Box and whisker plots of proportion of cells per indicated region with T cells belonging to the indicated
642 CD4 T cells clusters. Statistical testing by two-sided t-test (* <0.05, ** <0.01). Error bars represent standard
643 error of the mean.
644 B) Box and whisker plots of proportion of cells per indicated region with T cells belonging to the indicated
645 CD8 T cells clusters. Statistical testing by two-sided t-test (* <0.05, ** <0.01). Error bars represent standard
646 error of the mean.

647   C) Box and whisker plot of exhaustion score per cell in the indicated region types. Statistical testing by two-
648   sided t-test (**** <0.0001).
649   D,E) Flow cytometric quantification of %CD39 or PD-1 MFI on CD8 T cells across the indicated region
650   types. Statistical testing by two-sided t-test (** <0.01). Error bars represent standard error of the mean.
651   F) Paired box and whisker plots of average exhaustion score per clone that is matched between regions
652   without viable tumor and regions with viable tumor. Statistical testing by paired two-sided t-test. Error bars
653   represent standard error of the mean.
654   For A-F, only thoracic resection regions from MSK 1263 and 1302 were included in this analysis due to
655   simultaneous availability of adjacent normal, no viable tumor, viable tumor, and LN regions.
656   G) Photograph of H&E staining from two adrenal regions involved with tumor in MSK 1263 and the
657   associated CD39 and PD-1 flow cytometry plots gated on CD8 T cells.
658   H) Spearman correlation of indicated T cell clusters across the three patients. P-values of correlation are
659   indicated (* <0.05, ** <0.01).

Figure 3
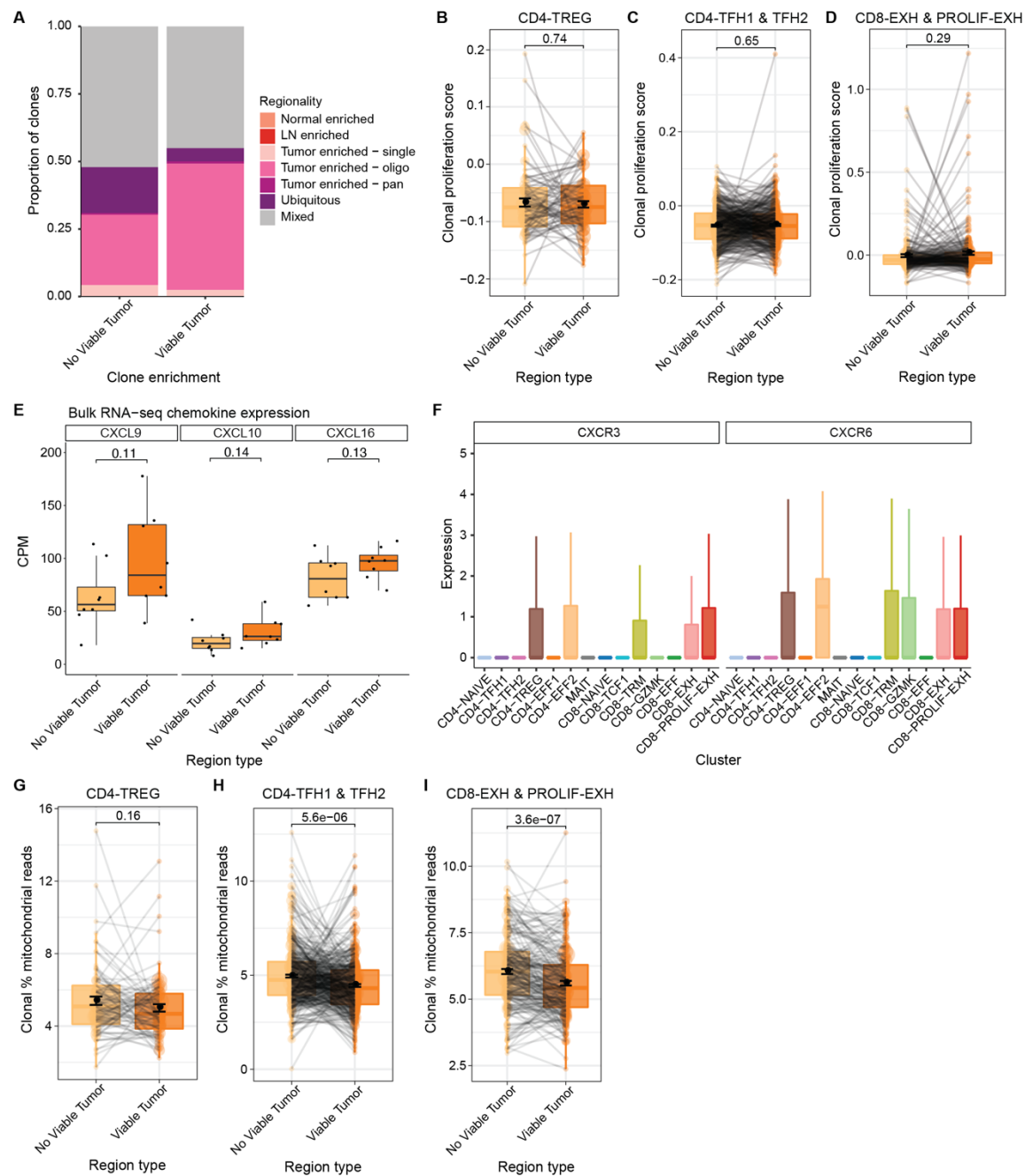
660
Figure 3. T cell proliferation, migration, and cell viability comparing tumor regions without and with viable cancer.

A) Bar plots of the proportion of clones enriched in tumor regions without or with viable cancer cells colored by their TCR regional pattern.

B-D) Paired box and whisker plot of average proliferation score per clone in the indicated phenotype subgroup that is matched between regions without viable tumor and regions with viable tumor. Statistical testing by two-sided t-test. Error bars represent standard error of the mean.

E) Expression of chemokines CXCL9, CXCL10, and CXCL16 among no viable and viable tumor regions as measured by bulk RNA-seq. Statistical testing by two-sided t-test. CPM = counts per million.

F) Expression of chemokine receptors CXCR3 and CXCR6 among scRNA-seq phenotypic clusters.

671   G-I) Paired box and whisker plot of average percent mitochondrial reads per clone in the indicated
672   phenotype subgroup that is matched between regions without viable tumor and regions with viable tumor.
673   Statistical testing by two-sided t-test. Error bars represent standard error of the mean.

Figure 4
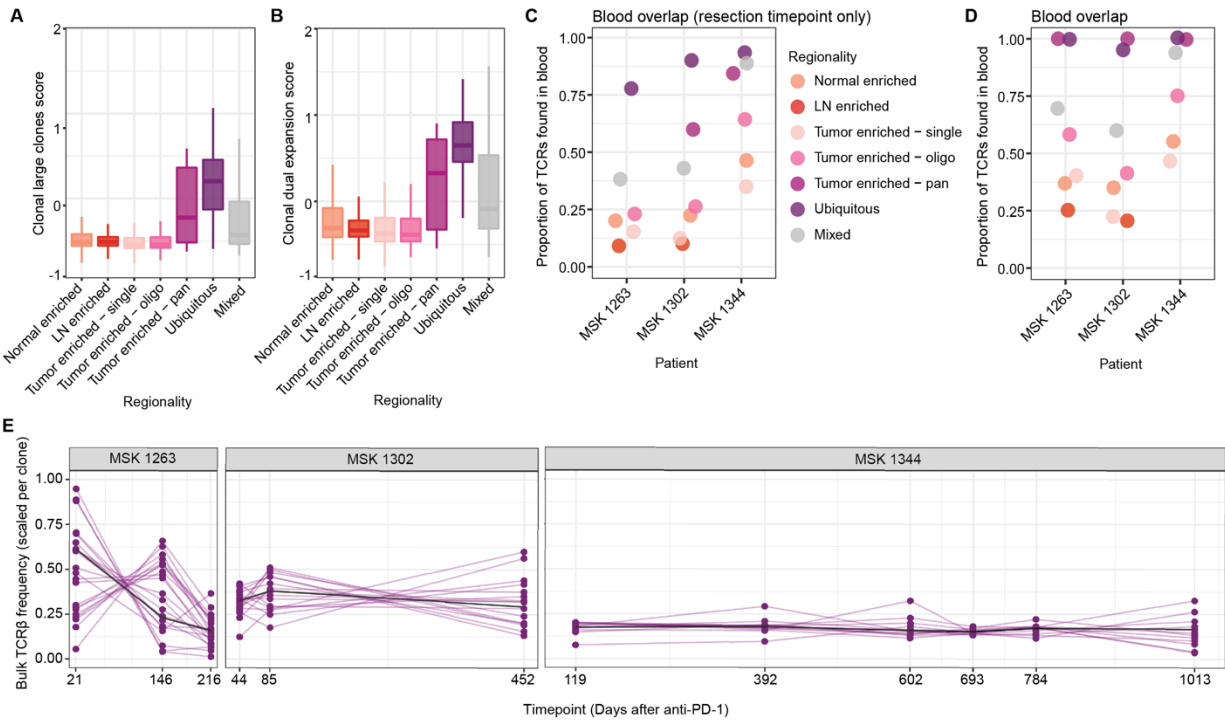
Figure 4. Peripheral T cell dynamics of clonotypes with ubiquitous phenotype.
A-B) Box and whisker plots of gene signature scores for 'large clones'[20] (A), or 'dual expansion'[14] (B) among clones with the indicated TCR regional pattern.
C,D) Percentage of clones with the indicated regional patterns for which a matched TCRβ sequence could be found in the peripheral blood at the time of resection (C) or at any time point surveyed (D).
E) Circulating frequency over time of ubiquitous TCR clones.

Figure 5
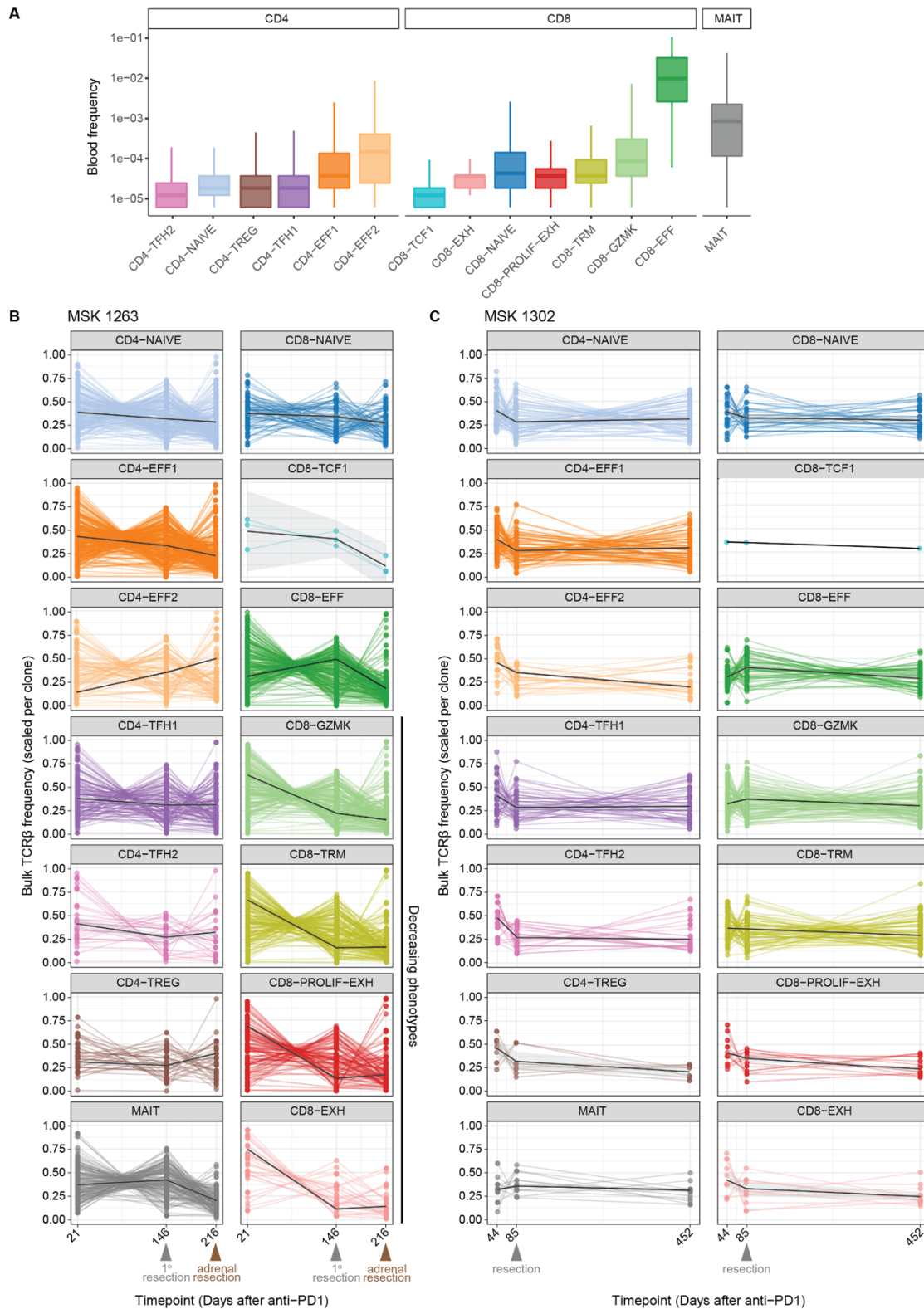
684   **Figure 5. Peripheral T cell dynamics of clonotypes associated with tissue T cell clusters.**
685   A) Circulating frequency of clonotypes with the indicated CD4, CD8, or MAIT clusters designated by tissue
686   scTCR/RNA-seq in MSK 1263, 1302, and 1344. Each clonotype was counted one time for each cell in the
687   cluster designation to which the cell belonged.
688   B,C) Circulating frequency over time of clonotypes from patient MSK 1263 (B) or MSK 1302 (C) associated
689   with the indicated CD4, CD8, or MAIT clusters designated by tissue scTCR/RNA-seq. Each clonotype was
690   counted one time for each cell in the cluster designation to which the cell belonged. Grey arrow represents
691   timepoint of primary oligometastatic resection; brown arrow represents timepoint of second oligometastatic
692   adrenal resection.

Figure 6
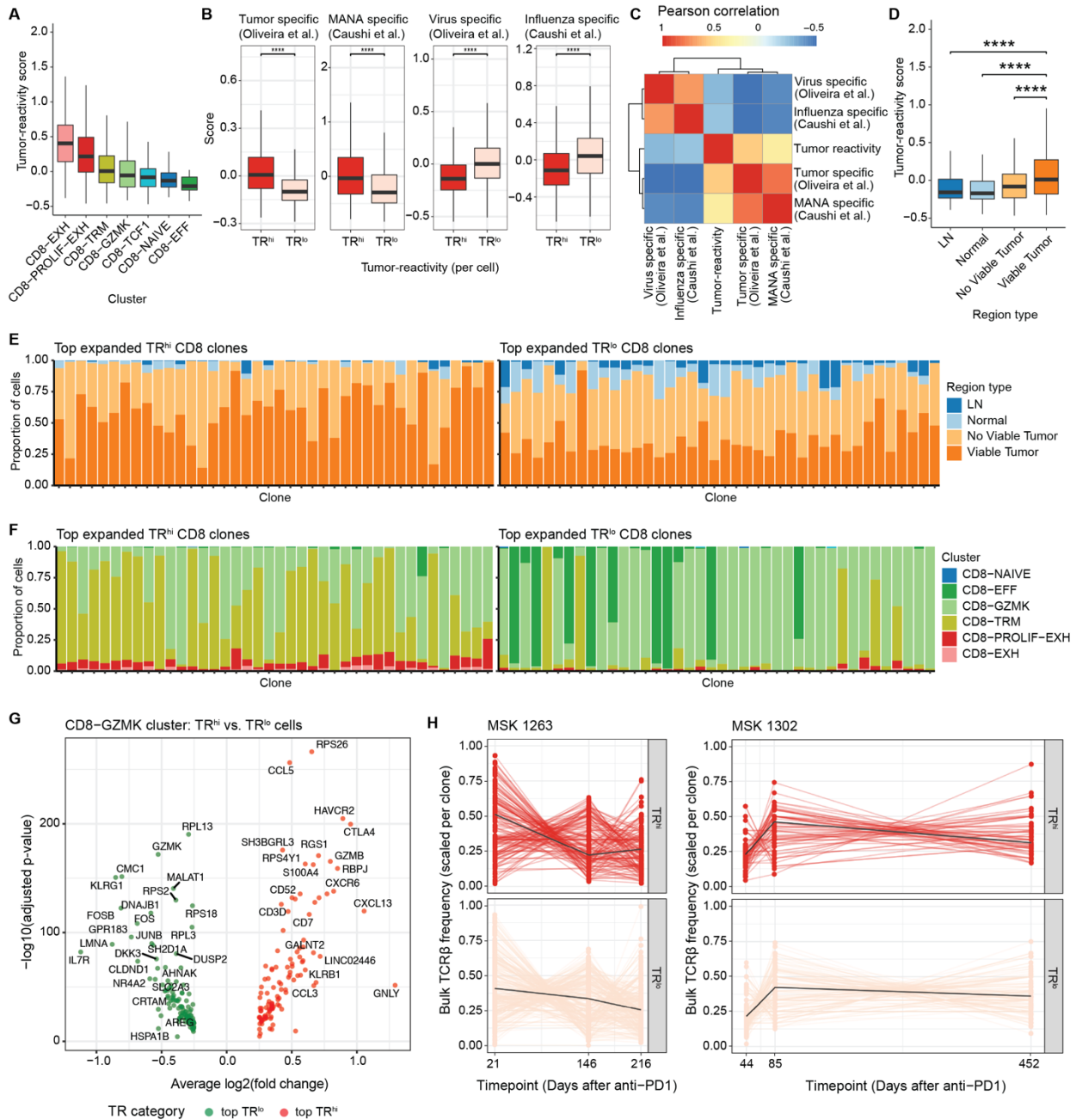
Figure 6. Peripheral T cell dynamics of clonotypes with high tumor-reactivity features.
A) Box and whisker plot of tumor-reactivity scores[22] among the indicated CD8 T cell clusters in MSK 1263, 1302, and 1344.
B) Box and whisker plots of 'tumor-specific'[28], 'MANA-specific'[27], 'virus-specific'[28], and 'influenza-specific'[27] scores among CD8 T cells with high (>0) and low (≤0) tumor-reactivity scores. Statistical testing by two-sided t-test (**** <0.0001).
C) Heat map of Pearson correlation matrix between tumor-reactivity score with 'tumor-specific', 'MANA-specific', 'virus-specific', and 'influenza-specific' scores computed on all cells.
D) Box and whisker plot of tumor-reactivity scores across the indicated region types. Statistical testing by two-sided t-test (**** <0.0001).

704   E) Bar plots of the proportion of cells in the indicated region type among the top 40 most expanded TR^{hi}
705   (left) or TR^{lo} (right) CD8 clones.
706   F) Bar plots of the proportion of cells in the indicated clusters among the top 40 most expanded TR^{hi} (left)
707   or TR^{lo} (right) CD8 clones.
708   G) Volcano plot of differentially expressed genes between CD8-GZMK cluster cells among TR^{hi} and TR^{lo}
709   clones.
710   H) Circulating frequency over time of TR^{hi} (top) and TR^{lo} (bottom) CD8 TCR clones from patients MSK 1263
711   (left) and MSK 1302 (right).

Figure 7
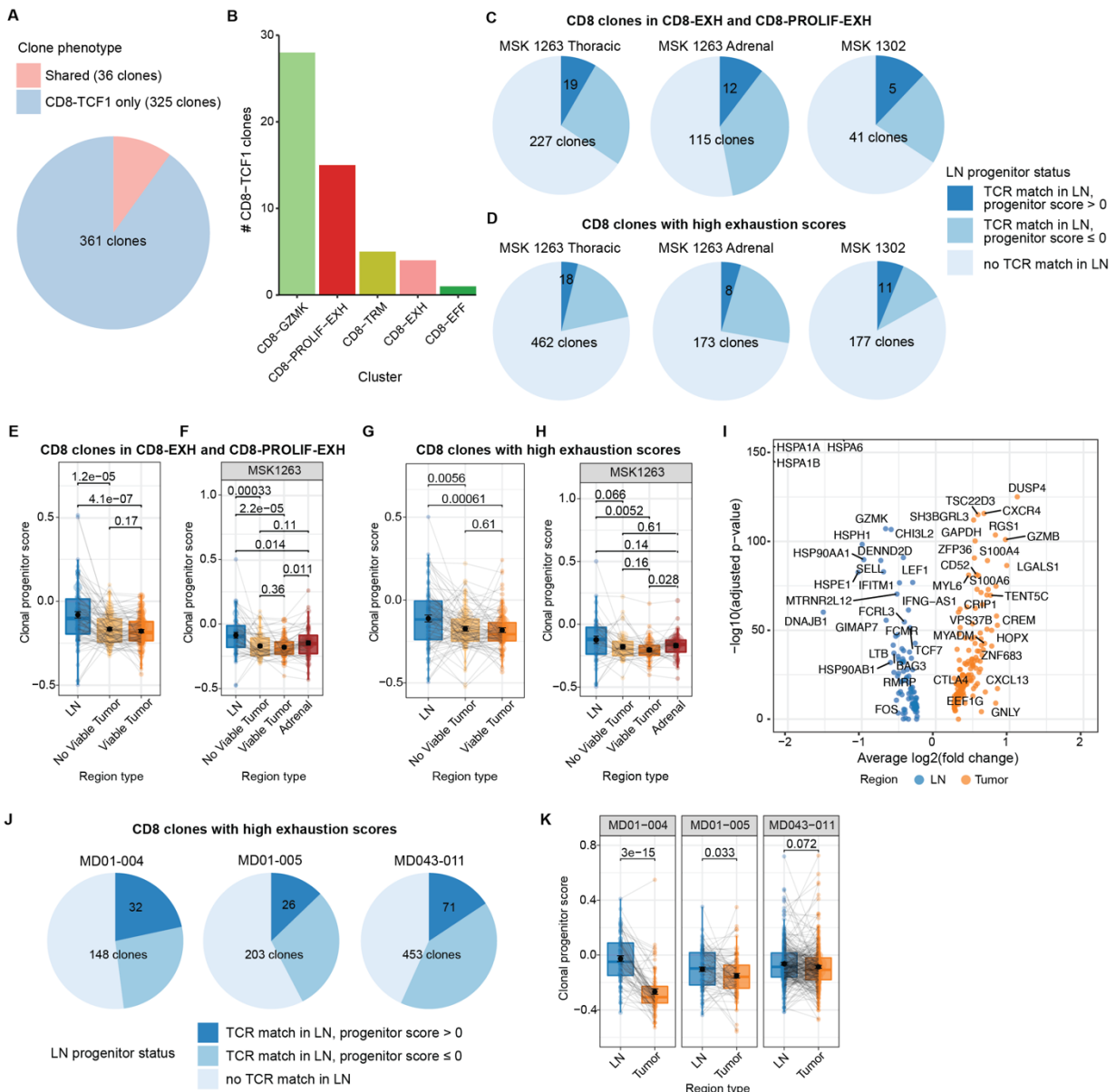
Figure 7. Intratumoral CD8 T cells can be found in a TCF-1⁺ precursor exhausted state in the regional LN.

A) Pie chart of clonotypes shared (pink) between CD8-TCF1 cluster and CD8 T cells in tumor regions, and clones found only in the CD8-TCF1 cluster (blue).

B) Bar plot of absolute number of CD8-TCF1 clones found within other CD8 clusters in the tumor.

C,D) Pie chart of CD8 T cell clones in the CD8-EXH and CD8-PROLIF-EXH clusters (C) or with high exhaustion scores (D) in the tumor that could be matched to a clonotype in the LN (medium blue and dark blue, "TCR match in LN"). Dark blue slice indicates that the matched clone could be found with a progenitor score >0 in the LN.

E,G) Paired box and whisker plots of average progenitor score per CD8 T cell clone in the CD8-EXH and CD8-PROLIF-EXH clusters (E) or with high exhaustion scores in thoracic regions of MSK 1263 and 1302 (G) that is matched among the LN, regions without viable tumor, and regions with viable tumor. Statistical testing by paired two-sided t-test. Error bars represent standard error of the mean.

726   F,H) Paired box and whisker plots of average progenitor score per CD8 T cell clone in the CD8-EXH and
727   CD8-PROLIF-EXH clusters (F) or with high exhaustion scores in thoracic regions of MSK 1263 (H) that is
728   matched among the LN, regions without viable tumor, regions with viable tumor, and resected adrenal
729   regions. Statistical testing by paired two-sided t-test. Error bars represent standard error of the mean.
730   I) Volcano plot of differentially expressed genes between cells from clone-matched CD8 T cell clones in the
731   LN and tumor.
732   J) Pie chart of CD8 T cell clones with high exhaustion scores in an external data set that could be matched
733   to a clonotype in the LN (medium blue and dark blue, "TCR match in LN"). Dark blue slice indicates that the
734   matched clone could be found with a progenitor score >0 in the LN.
735   K) Paired box and whisker plot of average progenitor score per clone in three separate patients from an
736   external dataset that is matched among the LN and tumor regions. Statistical testing by paired two-sided
737   t-test. Error bars represent standard error of the mean.

Figure S1 (related to Figure 1)
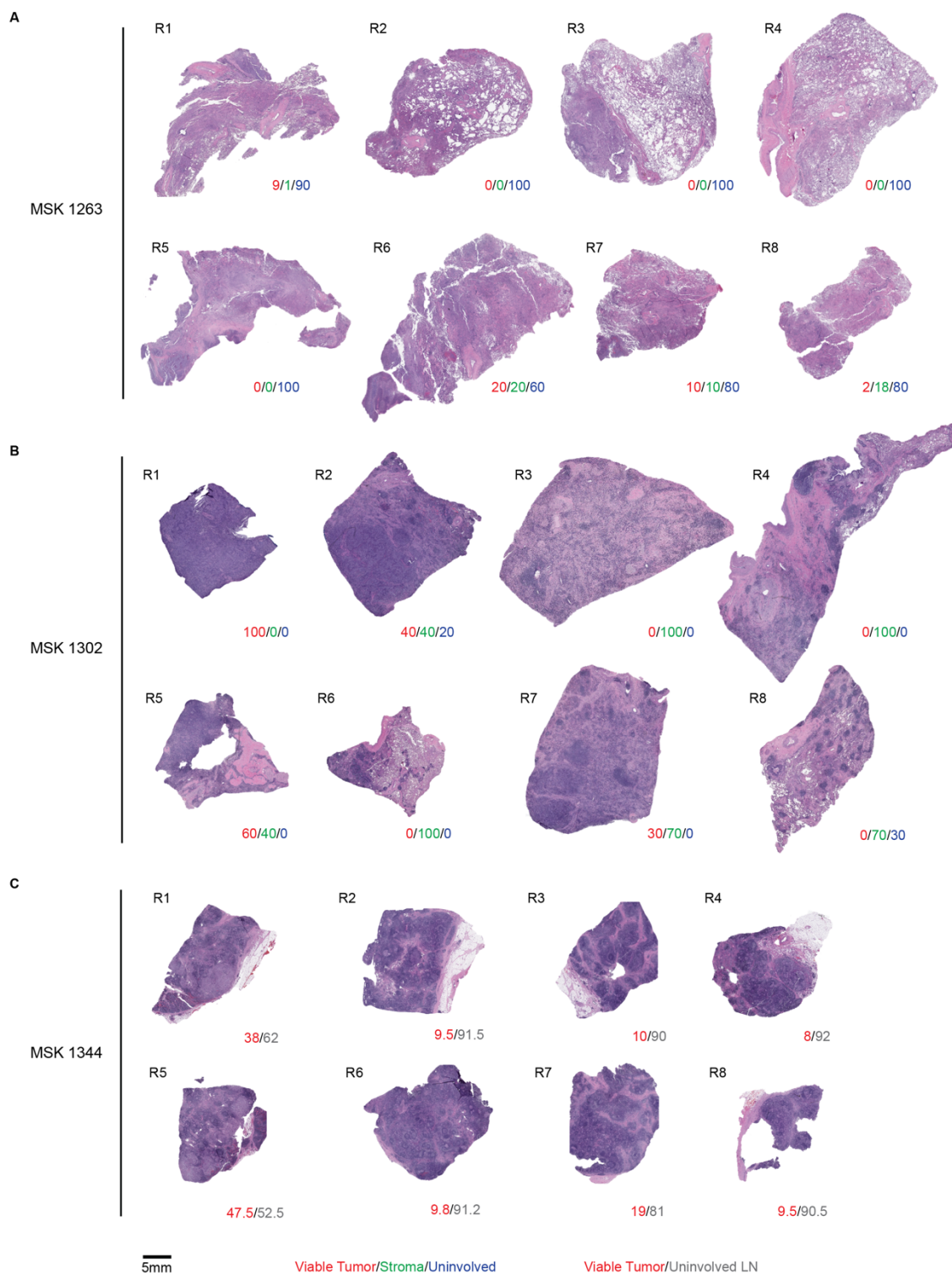
738
739 **Figure S1. Pathological heterogeneity among regional resections after ICB.**
740 A-C) Photographs of H&E-stained regions among primary tumor bed of resections from MSK 1263 (A),
741 1302 (B), and 1344 (C).

Figure S2 (related to Figure 1)
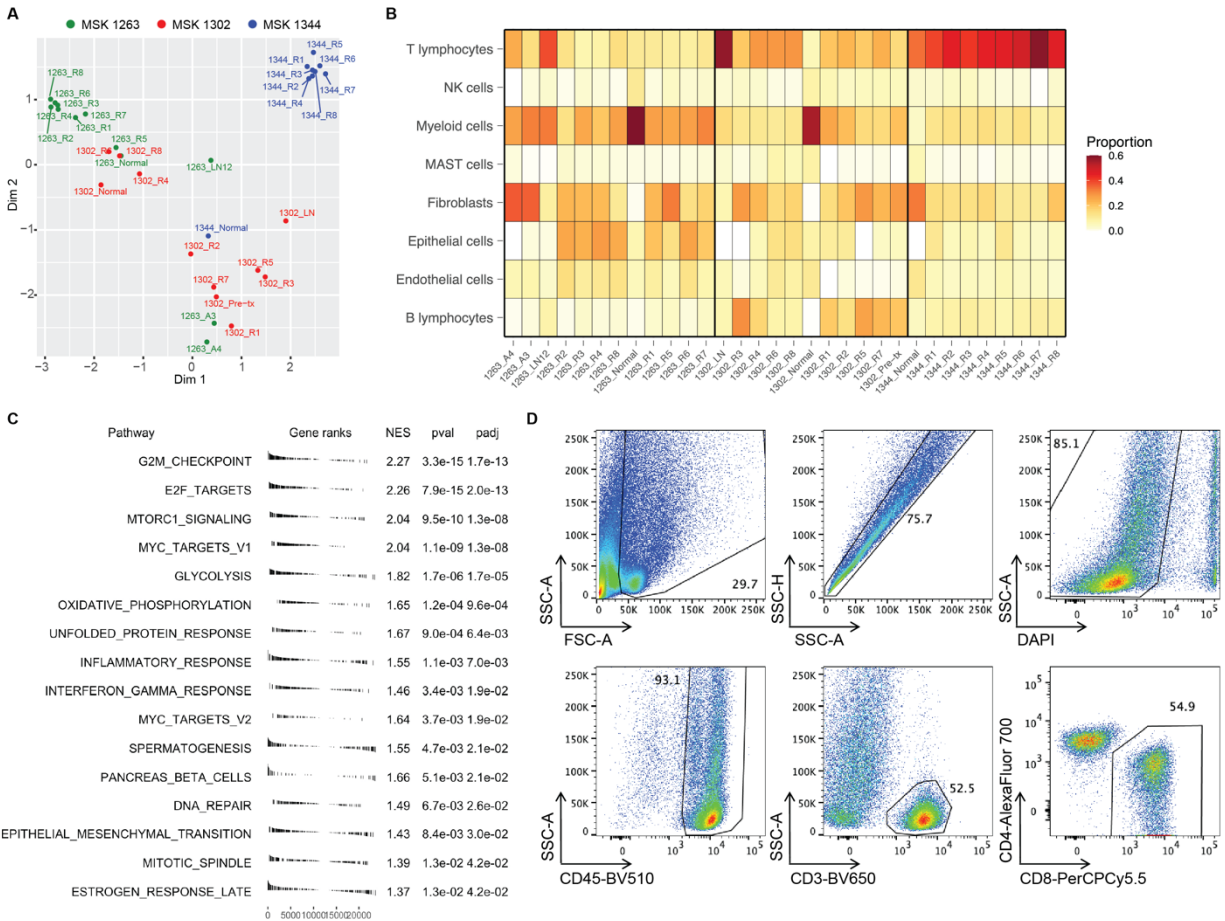
Figure S2. Regional transcriptional heterogeneity in resections after ICB.
A) Principal component analysis of bulk RNA sequencing of regions from three patients undergoing oligometastatic resections.
B) Heat map of CIBERSORT quantification of various immune populations (y-axis) across the different regions from three patients (x-axis).
C) GSEA of pathways differentially expressed among viable vs. no viable tumor regions as measured by bulk RNA-seq.
D) Representative gating strategy for the isolation of CD3+ T cells by flow cytometry.

Figure S3 (related to Figure 1)
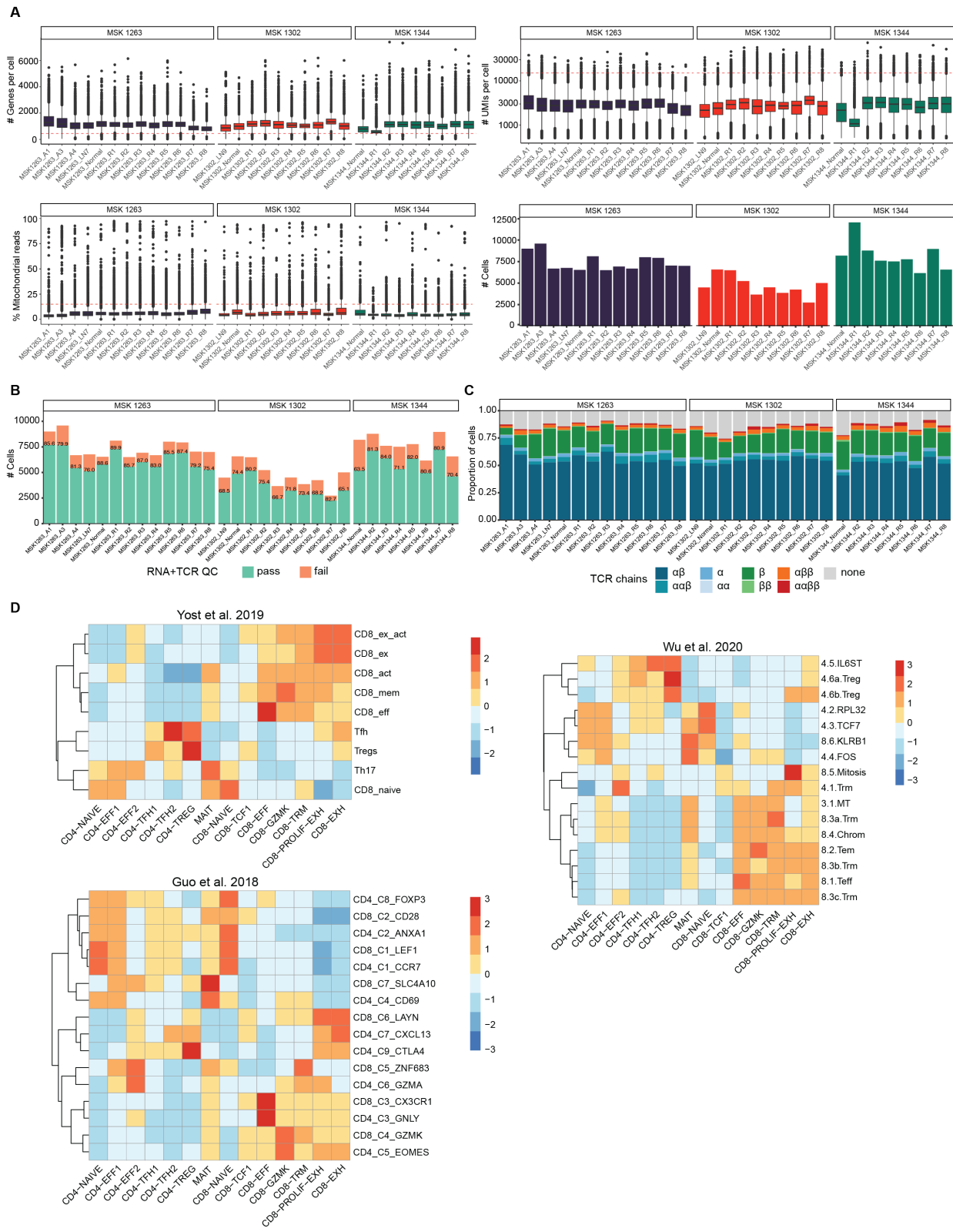
Figure S3. Quality control and comparison of cluster-defining genes to published scRNA-seq clusters.

A) Box and whisker plots of number of genes detected per cell, number of unique molecular identifiers (UMIs) per cell, percent mitochondrial reads per cell, and number of cells captured per region undergoing scTCR/RNA-seq. Cutoffs used for quality filtering are shown as dotted red lines.

B) Bar plot of absolute number of cells passing (green) and failing (orange) QC per region undergoing scTCR/RNA-seq.

C) Bar plot of absolute number of cells for which TCRα only (light blue), TCRβ only (green), or both TCRα and TCRβ chains (teal) were reconstructed per region undergoing scTCR/RNA-seq. T cells for which multiple TCRβ chains were captured (light green, orange, red) were excluded from further analysis.

D) Heat map comparing clusters designated in our dataset (x-axis) and clusters designated in the indicated external scRNA-seq datasets (y-axis). Color scale represents external cluster gene scores computed per cell in our dataset and normalized per row.

Figure S4 (related to Figure 1)
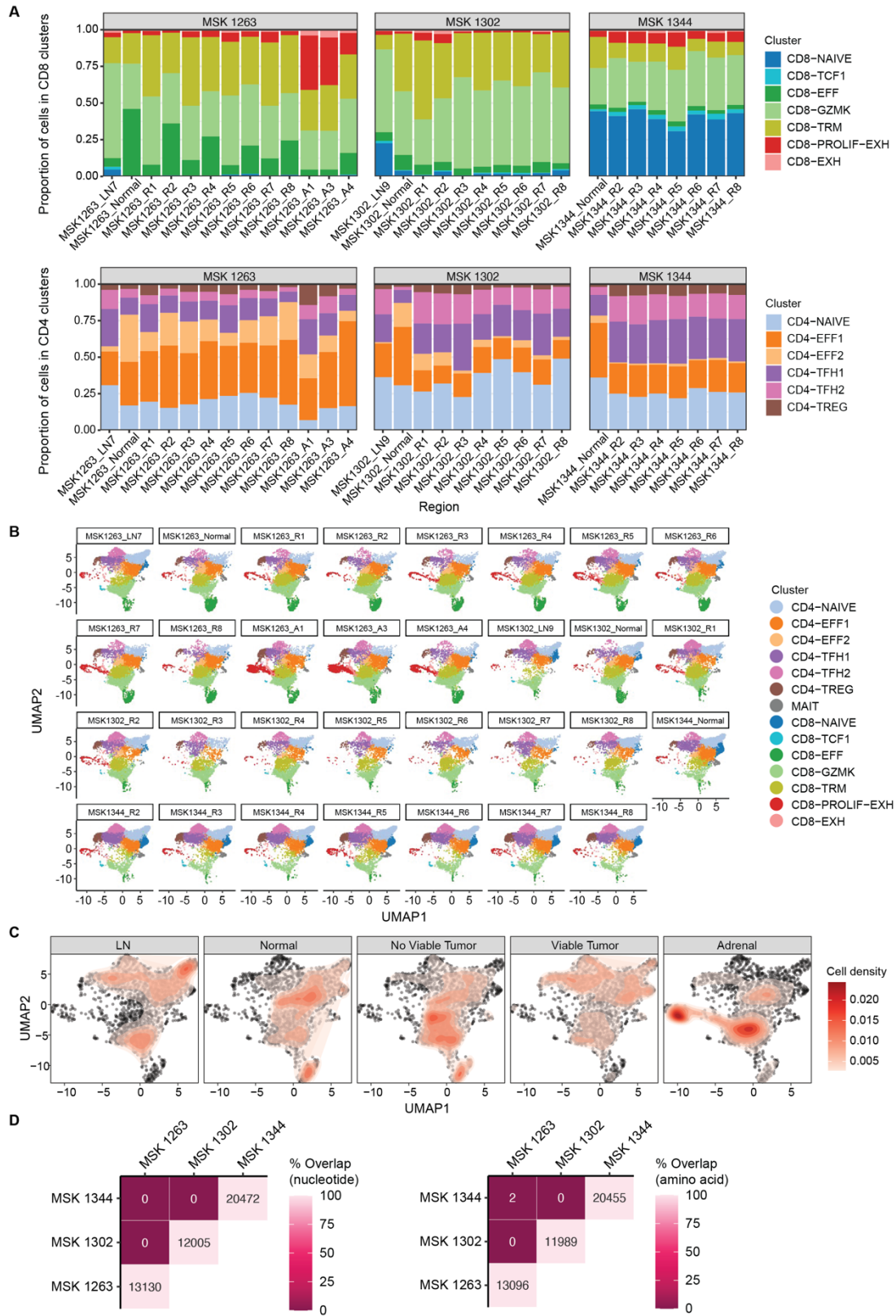
768   **Figure S4. Cluster and TCR clone representation across patients.**
769   A) Bar plots of the proportion of cells in the indicated clusters among CD4 T cells (top) or CD8 T cells
770   (bottom) per region undergoing scRNA-seq.
771   B) UMAP of cluster representation across the 31 regions undergoing scTCR/RNA-seq that passed QC.
772   C) UMAP of sorted CD3$^+$ T cells among each region type colored by cell density.
773   D) Heat map of TCR clonal overlap between patients based on CDR3αβ nucleotide (left) or amino acid
774   (right) sequence.

Figure S5 (related to Figure 2)
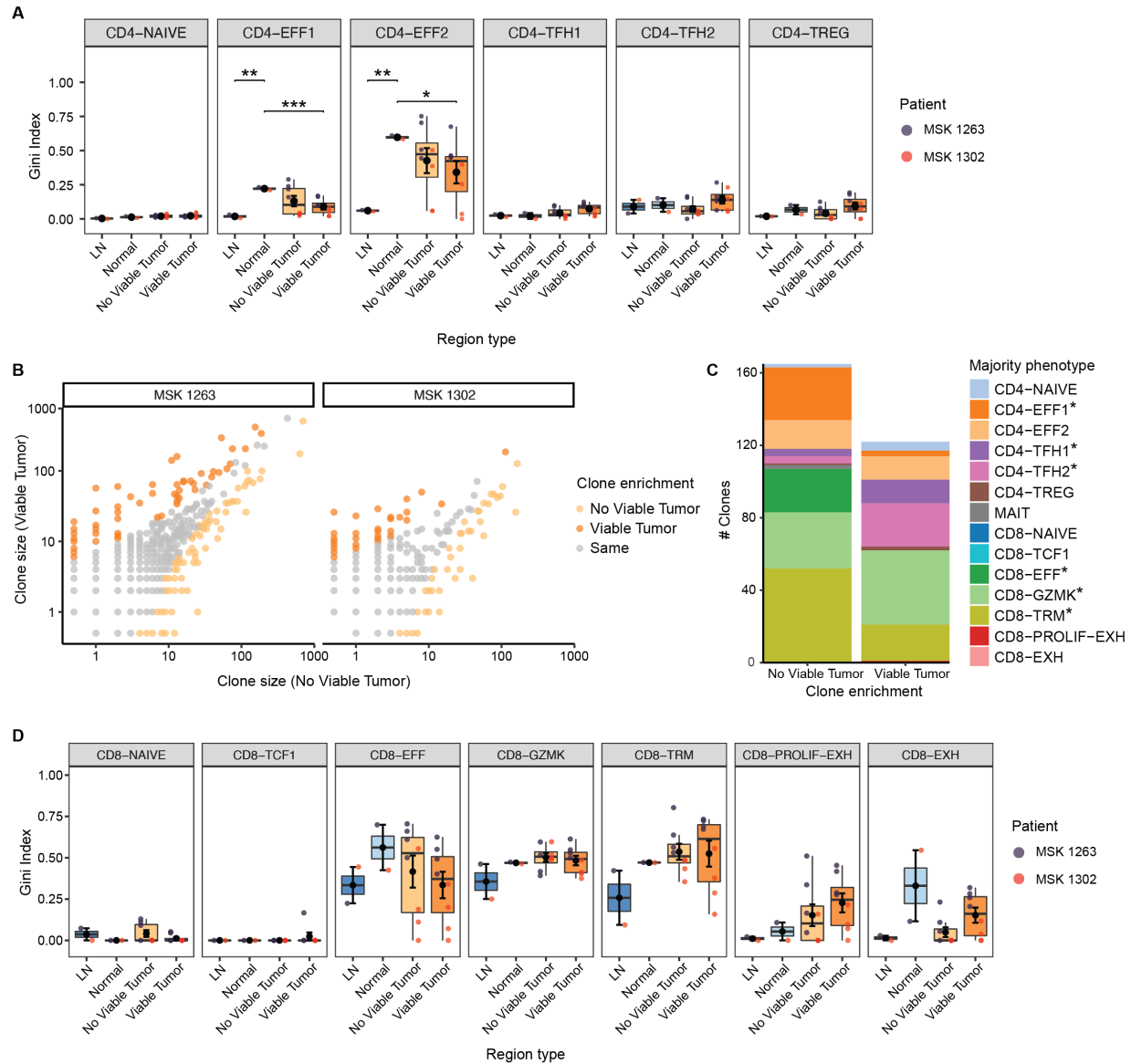
Figure S5. TCR clonal distribution across region types.

A) Box and whisker plots of Gini index of the indicated CD4 T cell clusters across region types. Statistical testing by two-sided t-test. Error bars represent standard error of the mean.

B) Scatterplot of the number of cells in regions with no viable tumor vs. regions with viable tumor. Each point represents one clone classified as enriched in viable tumor (dark orange) or no viable tumor (light orange) regions (Fisher's exact test, p<0.05).

C) Bar plot of clones enriched in no viable tumor regions or viable tumor regions, colored by majority phenotype within each clone. (* denotes significance as determined by Fisher's exact test, p<0.05).

D) Box and whisker plots of Gini index of the indicated CD8 T cell clusters across region types. Error bars represent standard error of the mean.

Figure S6 (related to Figures 3 and 4)
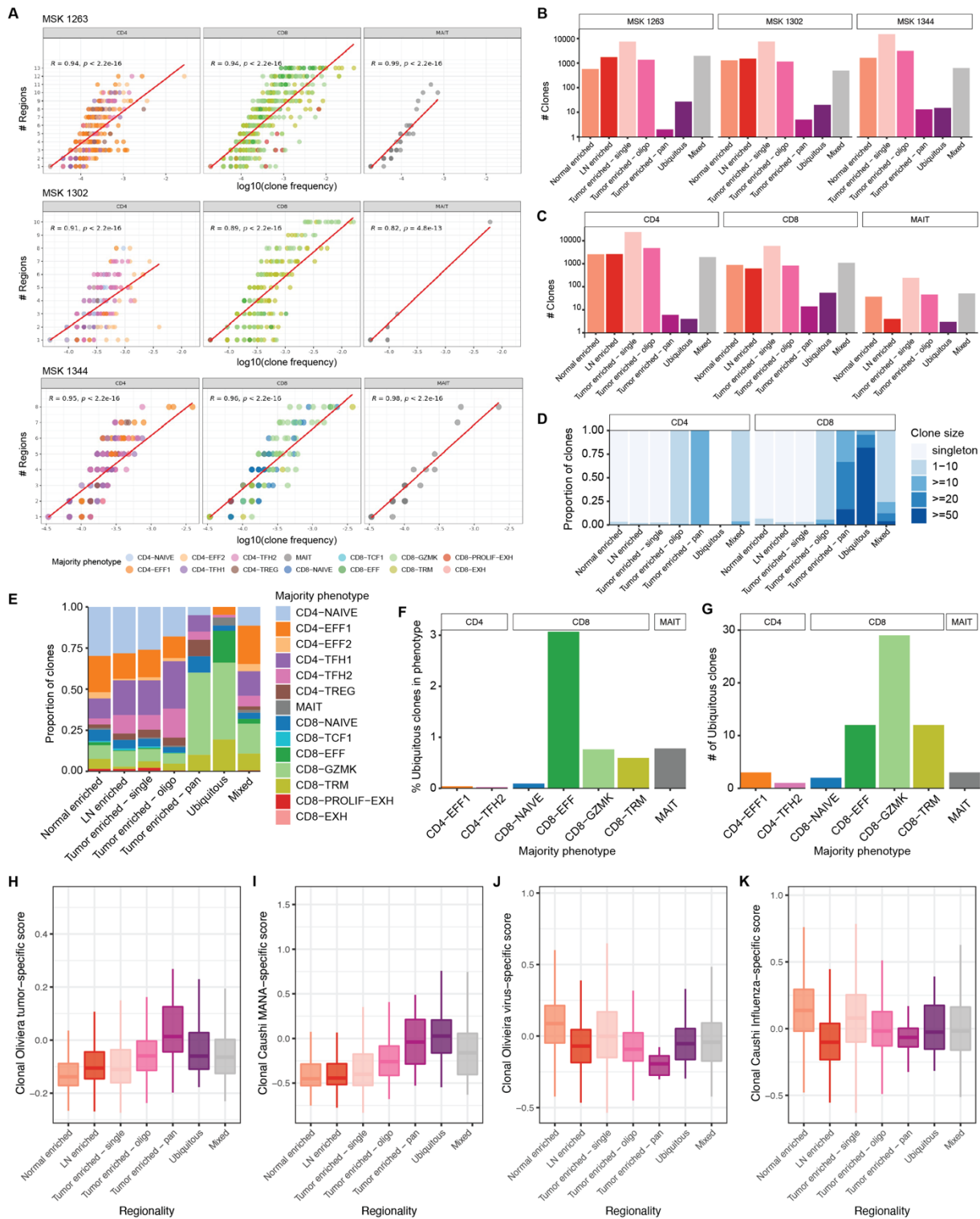
Figure S6. Regional patterns of TCR clones.
A) Spearman correlation per patient of indicated CD4, CD8, and MAIT clusters comparing the number of regions in which a T cell clone was detected and its clonal frequency in the sample's respective scTCR/RNA-seq dataset.

791   B) Bar plot of the number of clones within each non-overlapping TCR regional pattern per patient.

792   C) Bar plot of the number of clones within each non-overlapping TCR regional pattern per CD4, CD8, or
793   MAIT subset among all patients.

794   D) Bar plots of the proportion of clones with the indicated clone sizes per TCR regional pattern of CD4 and
795   CD8 T cell clones among all patients.

796   E) Bar plots of the proportion of clones with the indicated clusters per TCR regional pattern among all
797   patients.

798   F) Bar plots of the percentage of T cell clones with the indicated majority phenotype cluster designation that
799   exhibit the ubiquitous TCR regional pattern.

800   G) Bar plots of the absolute number of ubiquitous T cell clones with the indicated majority cluster
801   designation.

802   H-K) Box and whisker plots of 'tumor-specific'[28] (H), 'MANA-specific'[27] (I), 'virus-specific'[28] (J), and
803   'influenza-specific'[27] (K) scores among T cell clones with the indicated TCR regional pattern.

Figure S7 (related to Figure 3)
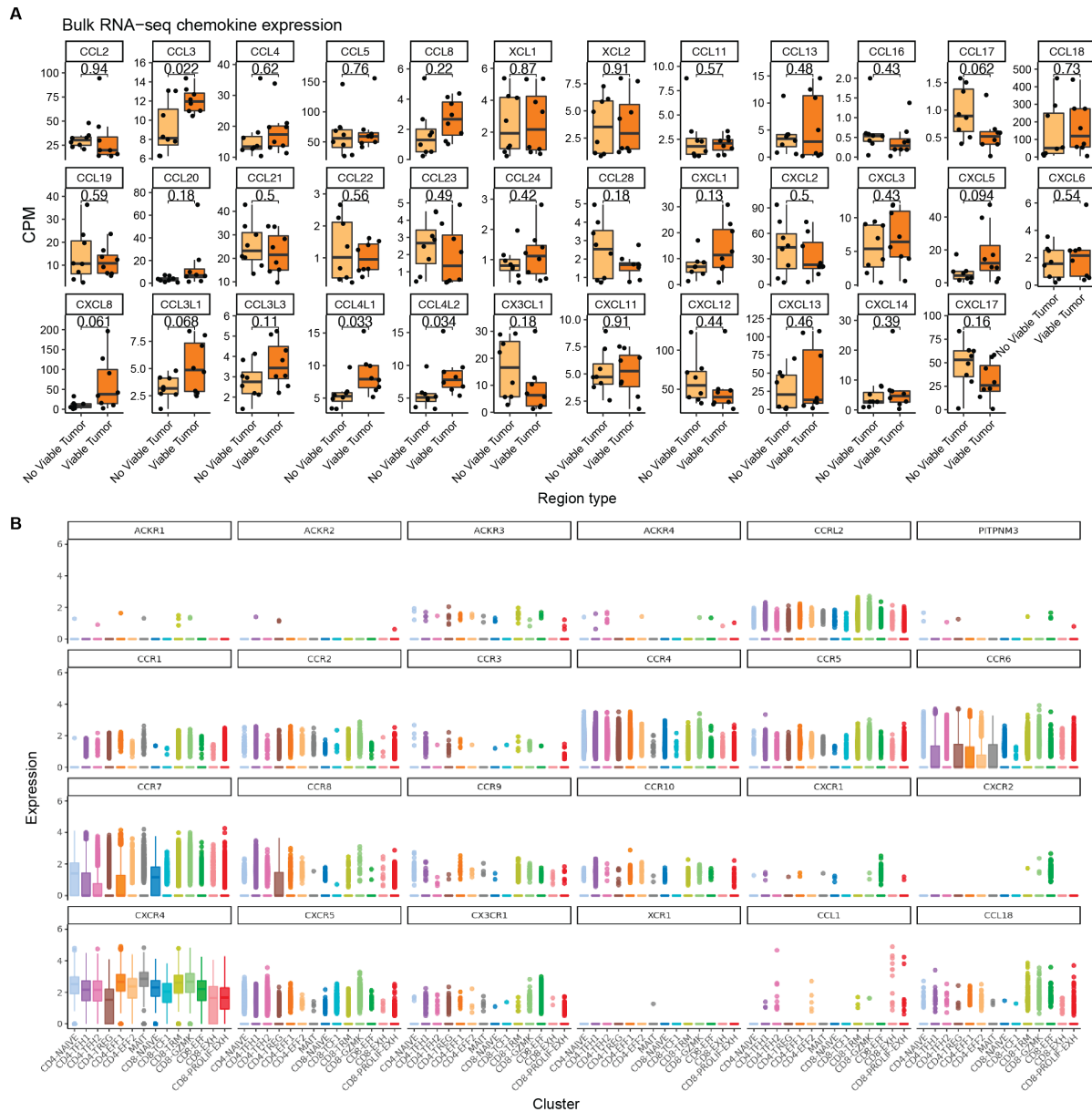
804
Figure S7. Chemokine ligand and receptor expression.
805
A) Expression of chemokines among no viable and viable tumor regions as measured by bulk RNA-seq.
806
Statistical testing by t-test. CPM = counts per million. Statistical testing by two-sided t-test.
807
B) Expression of chemokine receptors among scRNA-seq phenotypic clusters.
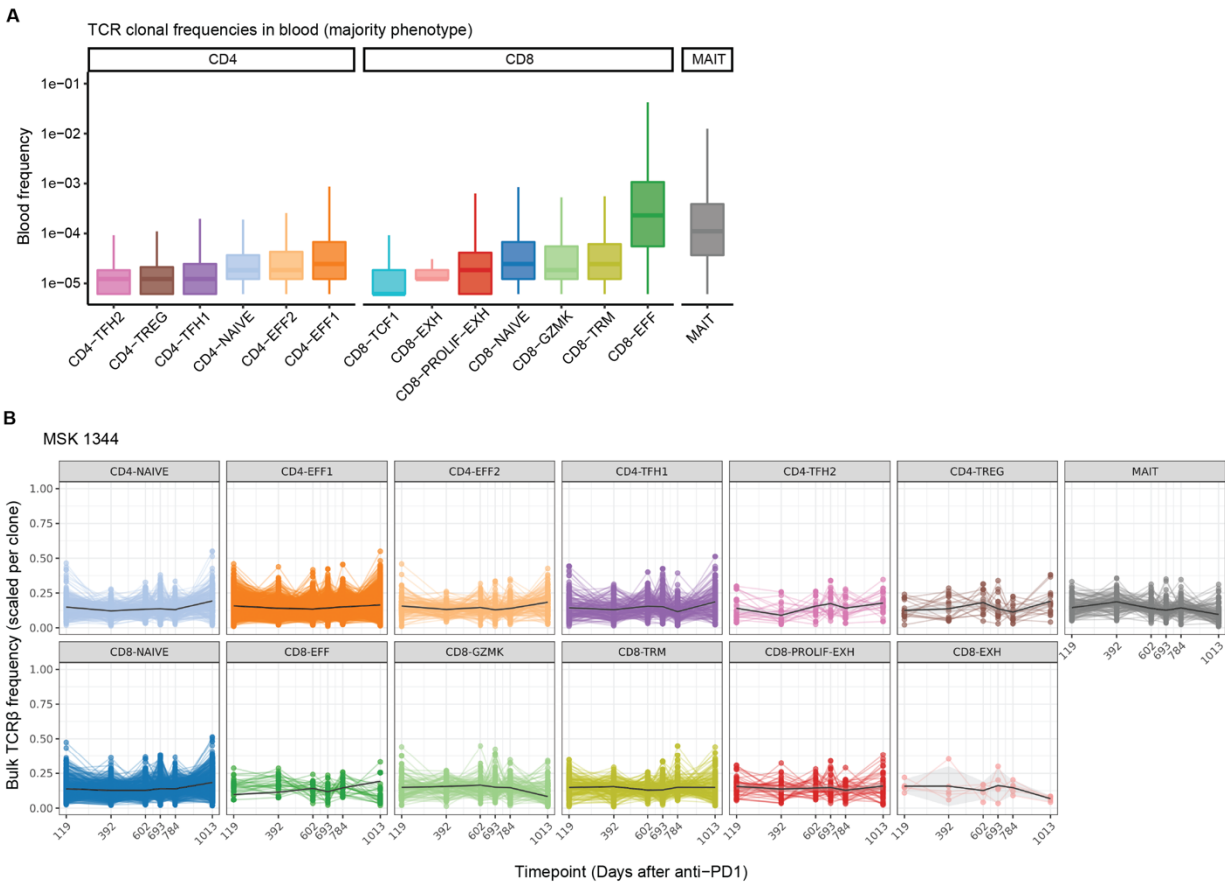808

Figure S8 (related to Figure 4)
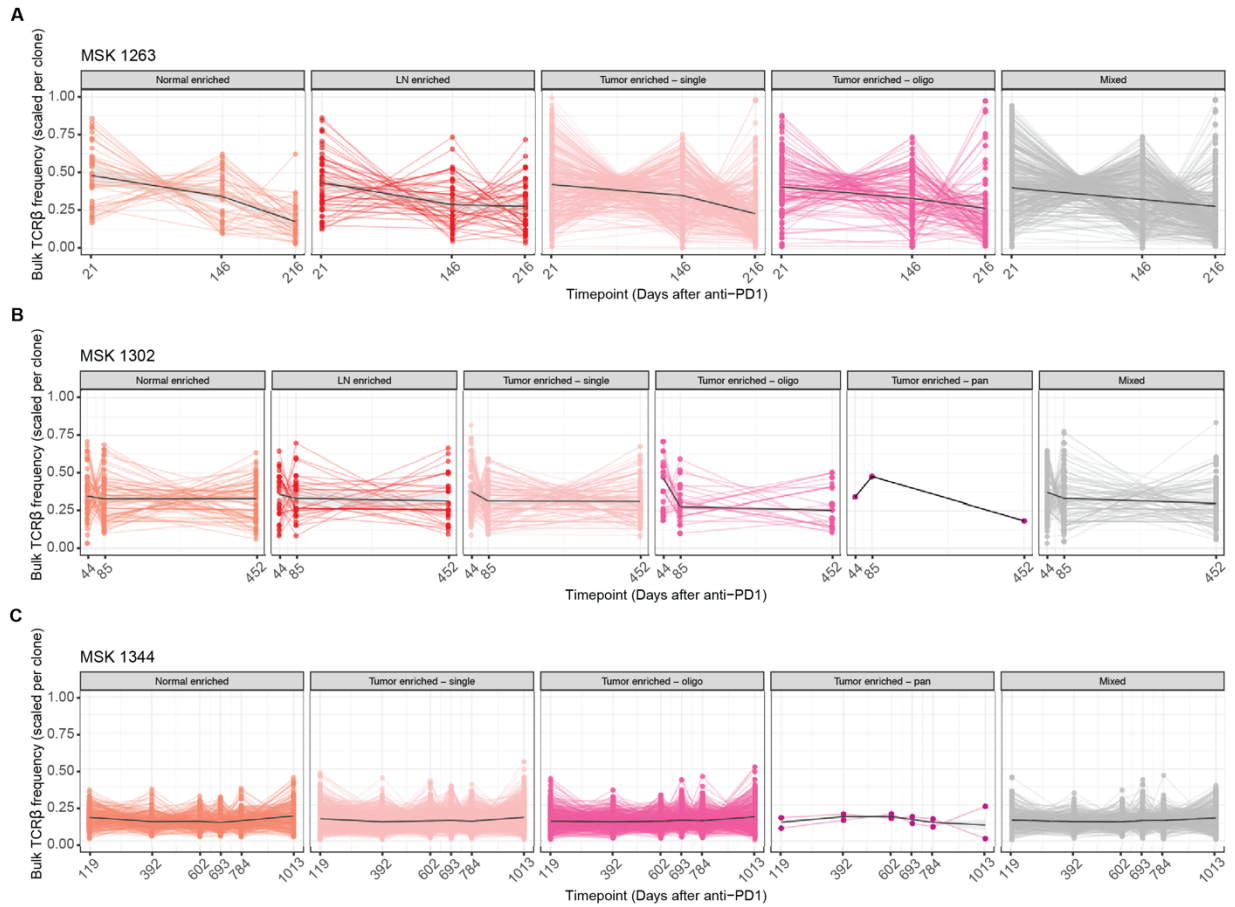
809
810 **Figure S8. Peripheral T cell dynamics of non-ubiquitous T cell clones.**
811 A-C) Circulating frequency over time of TCR clones from MSK 1263 (A), 1302 (B), or 1344 (C) with non-
812 ubiquitous TCR regional patterns.

Figure S9 (related to Figure 5)

813
814 **Figure S9. Peripheral T cell dynamics of clonotypes associated with tissue T cell clusters.**
815 A) Circulating frequency of clonotypes with the indicated CD4, CD8, or MAIT clusters designated by tissue
816 scTCR/RNA-seq. Each clonotype was counted only one time in the cluster in which the majority of cells in
817 the clone resided.
818 B) Circulating frequency over time of clonotypes from patient MSK 1344 associated with the indicated CD4,
819 CD8, or MAIT clusters designated by tissue scTCR/RNA-seq. Each clonotype was counted one time for
820 each cell in the cluster designation to which the cell belonged.

Figure S10 (related to Figure 6)
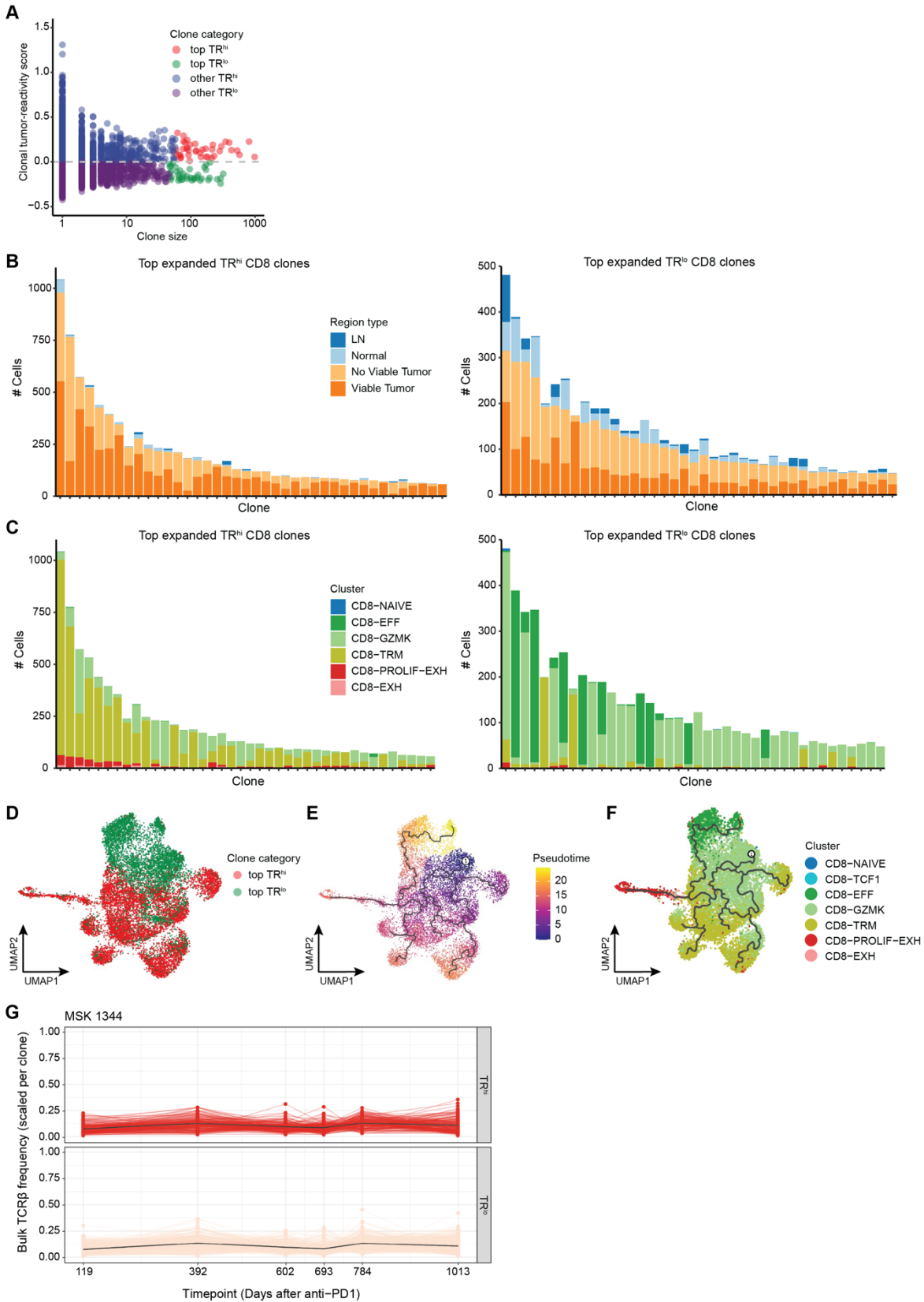
822   **Figure S10. Characterization of TR^{hi} and TR^{lo} CD8 T cell clones.**

823   A) Scatterplot of clone size and tumor-reactivity score per clone, colored by tumor-reactivity category. 'Top

824   TR^{hi}' and 'top TR^{lo}' represent the 40 most expanded TR^{hi} or TR^{lo} CD8 clones, respectively.

825   B) Absolute number of cells in the indicated region types among the top 40 most expanded TR^{hi} (left) or

826   TR^{lo} (right) CD8 clones.

827   C) Absolute number of cells in the indicated clusters among the top 40 most expanded TR^{hi} (left) or TR^{lo}

828   (right) CD8 clones.

829   D-F) Trajectory analysis comparing TR^{hi} and TR^{lo} CD8 T cell clones. UMAP of cells from the top 40 most

830   expanded TR^{hi} and TR^{lo} CD8 clones colored by tumor-reactivity category (D), pseudotime (E), or phenotype

831   cluster (F).

832   G) Circulating frequency over time of TR^{hi} (top) and TR^{lo} (bottom) TCR clones from MSK 1344.

Figure S11 (related to Figure 7)
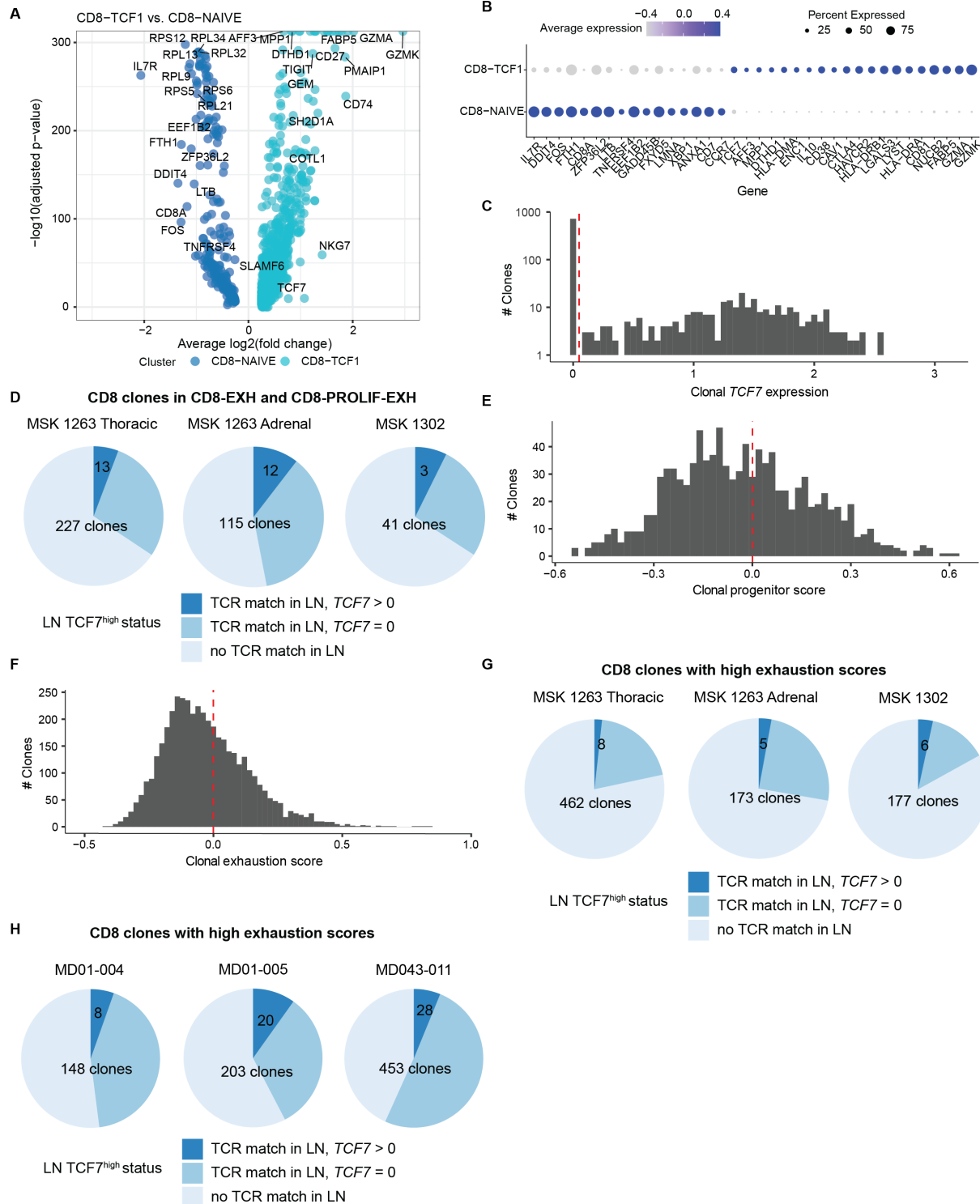
Figure S11. Identification of LN progenitor states.
A) Volcano plot of differentially expressed genes between clusters CD8-TCF1 and CD8-NAÏVE.
B) Dot plot of select differentially expressed genes between clusters CD8-TCF1 and CD8-NAÏVE colored by average expression. Dot sizes represent the percent of cells expressing the indicated gene.
C) Distribution of average *TCF7* expression among CD8 clones in LN regions.

839   D) Pie chart of CD8 T cell clones in the CD8-EXH and CD8-PROLIF-EXH clusters in the tumor that could
840   be matched to a clonotype in the LN (medium blue and dark blue, "TCR match in LN"). Dark blue slice
841   indicates that the matched clone could be found expressing *TCF7* in the LN.
842   E) Distribution of average progenitor score among CD8 clones in LN regions.
843   F) Distribution of average exhaustion score among CD8 clones in tumor tissue regions. Clones with an
844   average exhaustion score >0 were defined as CD8 clones with high exhaustion scores.
845   G,H) Pie chart of CD8 T cell clones with high exhaustion scores in the tumor that could be matched to a
846   clonotype in the LN (medium blue and dark blue, "TCR match in LN") based on our scRNA/TCR-seq dataset
847   (G) or the dataset generated by Caushi et al[27] (H). Dark blue slice indicates that the matched clone could
848   be found expressing *TCF7* in the LN.

864
865 **AUTHOR CONTRIBUTIONS:** JAP conceived the project, analyzed the data, drafted and edited the
866 manuscript. AC conceived the project, performed and analyzed experiments, drafted and edited the
867 manuscript. MM, HR, NS, FZU, AQV, JMC, PM, VA and JC performed experiments and/or helped in
868 procurement of biospecimens. JLS provided pathologic analyses of the resected tissues. AJP provided
869 radiographic analyses of the tissues. HJW analyzed experiments. HW, MD, BHL, DQ, EdS, TS, JDW, TM,
870 CMR supervised portions of the study. ATS and MDH conceived the project and supervised the study.
871
872 **DECLARATION OF INTERESTS:** JDW is a consultant for Adaptive Biotech, Amgen, Apricity, Ascentage
873 Pharma, Arsenal IO, Astellas, AstraZeneca, Bayer, Beigene, Boehringer Ingelheim, Bristol Myers Squibb,
874 Celgene, Chugai, Daiichi Sankyo, Dragonfly, Eli Lilly, Elucida, F Star, Georgiamune, Idera, Imvaq, Kyowa
875 Hakko Kirin, Linneaus, Maverick Therapeutics, Merck, Neon Therapeutics, Polynoma, Psioxus, Recepta,
876 Takara Bio, Trieza, Truvax, Trishula, Sellas, Serametrix, Surface Oncology, Syndax, Syntalogic, and
877 Werewolf Therapeutics. JDW has received grant/research support from Bristol Myers Squibb and Sephora.
878 JDW has equity in Tizona Pharmaceuticals, Adaptive Biotechnologies, Imvaq, Beigene, Linneaus, Apricity,
879 Arsenal IO, and Georgiamune. JDW is a co-inventor on patent applications related to heteroclitic cancer
880 vaccines and recombinant poxviruses for cancer immunotherapy. JDW and TM are co-inventors on patent
881 applications related to CD40 and in situ vaccination (PCT/US2016/045970). TM is a consultant for Immunos
882 Therapeutics and Pfizer. TM is a cofounder of and equity holder in IMVAQ Therapeutics. TM receives
883 research funding from Bristol-Myers Squibb, Surface Oncology, Kyn Therapeutics, Infinity Pharmaceuticals,
884 Peregrine Pharmaceuticals, Adaptive Biotechnologies, Leap Therapeutics, and Aprea Therapeutics. TM is
885 an inventor on patent applications related to work on oncolytic viral therapy, alpha virus–based vaccine,
886 neoantigen modeling, CD40, GITR, OX40, PD-1, and CTLA-4. C.M.R. has consulted regarding oncology
887 drug development with AbbVie, Amgen, Ascentage, AstraZeneca, BMS, Celgene, Daiichi Sankyo,
888 Genentech/Roche, Ipsen, Loxo and PharmaMar and is on the scientific advisory boards of Elucida, Bridge
889 and Harpoon. Unrelated to this work, D.Z. reports clinical research support to his institution from Astra
890 Zeneca, Plexxikon, and Genentech; and personal/consultancy fees from Merck, Synlogic Therapeutics,
891 GSK, Genentech, Xencor, Memgen, Immunos, CrownBio, and Agenus. MDH received research grant from
892 BMS; personal fees from Achilles, Arcus, AstraZeneca, Blueprint, BMS, Genentech/Roche, Genzyme,
893 Immunai, Instil Bio, Janssen, Merck, Mirati, Natera, Nektar, Pact Pharma, Regeneron, Shattuck Labs,
894 Syndax, as well as equity options from Arcus, Factorial, Immunai, and Shattuck Labs. A.T.S. is a founder
895 of Immunai and Cartography Biosciences and receives research funding from Arsenal Biosciences,
896 Allogene Biotherapeutics, and 10x Genomics. A patent filed by MSKCC related to the use of tumor
897 mutational burden to predict response to immunotherapy (PCT/US2015/062208) is pending and licensed
898 by PGDx.
899
900
901
902
903
904

REFERENCES

1. Yost, K.E., Chang, H.Y. & Satpathy, A.T. Recruiting T cells in cancer immunotherapy. *Science* **372**, 130-131 (2021).

2. Hiam-Galvez, K.J., Allen, B.M. & Spitzer, M.H. Systemic immunity in cancer. *Nat Rev Cancer* (2021).

3. Osorio, J.C.*, et al.* Lesion-Level Response Dynamics to Programmed Cell Death Protein (PD-1) Blockade. *J Clin Oncol* **37**, 3546-3555 (2019).

4. Jia, Q.*, et al.* Local mutational diversity drives intratumoral immune heterogeneity in non-small cell lung cancer. *Nat Commun* **9**, 5361 (2018).

5. Sinjab, A.*, et al.* Resolving the Spatial and Cellular Architecture of Lung Adenocarcinoma by Multiregion Single-Cell Sequencing. *Cancer Discov* (2021).

6. Pai, J.A. & Satpathy, A.T. High-throughput and single-cell T cell receptor sequencing technologies. *Nat Methods* (2021).

7. Kallies, A., Zehn, D. & Utzschneider, D.T. Precursor exhausted T cells: key to successful immunotherapy? *Nat Rev Immunol* **20**, 128-136 (2020).

8. Connolly, K.A.*, et al.* A reservoir of stem-like CD8+ T cells in the tumor-draining lymph node preserves the ongoing anti-tumor immune response. *Science Immunology* **0**, abg7836.

9. Krishna, S.*, et al.* Stem-like CD8 T cells mediate response of adoptive cell immunotherapy against human cancer. *Science* **370**, 1328-1334 (2020).

10. Rafiq, S., Hackett, C.S. & Brentjens, R.J. Engineering strategies to overcome the current roadblocks in CAR T cell therapy. *Nat Rev Clin Oncol* **17**, 147-167 (2020).

11. Stuart, T.*, et al.* Comprehensive Integration of Single-Cell Data. *Cell* **177**, 1888-1902 e1821 (2019).

12. Guo, X.*, et al.* Global characterization of T cells in non-small-cell lung cancer by single-cell sequencing. *Nat Med* **24**, 978-985 (2018).

13. Yost, K.E.*, et al.* Clonal replacement of tumor-specific T cells following PD-1 blockade. *Nat Med* **25**, 1251-1259 (2019).

14. Wu, T.D.*, et al.* Peripheral T cell expansion predicts tumour infiltration and clinical response. *Nature* **579**, 274-278 (2020).

15. Ghorani, E.*, et al.* The T cell differentiation landscape is shaped by tumour mutations in lung cancer. *Nat Cancer* **1**, 546-561 (2020).

16. Gueguen, P.*, et al.* Contribution of resident and circulating precursors to tumor-infiltrating CD8(+) T cell populations in lung cancer. *Sci Immunol* **6**(2021).

17. Joshi, K.*, et al.* Spatial heterogeneity of the T cell receptor repertoire reflects the mutational landscape in lung cancer. *Nat Med* **25**, 1549-1559 (2019).

18. Li, H.*, et al.* Dysfunctional CD8 T Cells Form a Proliferative, Dynamically Regulated Compartment within Human Melanoma. *Cell* (2018).

19. Philip, M. & Schietinger, A. CD8(+) T cell differentiation and dysfunction in cancer. *Nat Rev Immunol* (2021).

20. Fairfax, B.P.*, et al.* Peripheral CD8(+) T cell characteristics associated with durable responses to immune checkpoint blockade in patients with metastatic melanoma. *Nat Med* **26**, 193-199 (2020).

21. Larson, R.C. & Maus, M.V. Recent advances and discoveries in the mechanisms and functions of CAR T cells. *Nat Rev Cancer* **21**, 145-161 (2021).

22. van der Leun, A.M., Thommen, D.S. & Schumacher, T.N. CD8(+) T cell states in human cancer: insights from single-cell analysis. *Nat Rev Cancer* **20**, 218-232 (2020).

23. Gros, A.*, et al.* PD-1 identifies the patient-specific CD8(+) tumor-reactive repertoire infiltrating human tumors. *J Clin Invest* **124**, 2246-2259 (2014).

24. Thommen, D.S.*, et al.* A transcriptionally and functionally distinct PD-1(+) CD8(+) T cell pool with predictive potential in non-small-cell lung cancer treated with PD-1 blockade. *Nat Med* **24**, 994-1004 (2018).

25. Duhen, T.*, et al.* Co-expression of CD39 and CD103 identifies tumor-reactive CD8 T cells in human solid tumors. *Nat Commun* **9**, 2724 (2018).

26. Simoni, Y.*, et al.* Bystander CD8(+) T cells are abundant and phenotypically distinct in human tumour infiltrates. *Nature* **557**, 575-579 (2018).

960   27.   Caushi, J.X.*, et al.* Transcriptional programs of neoantigen-specific TIL in anti-PD-1-treated lung
961   cancers. *Nature* (2021).
962   28.   Oliveira, G.*, et al.* Phenotype, specificity and avidity of antitumour CD8(+) T cells in melanoma.
963   *Nature* **596**, 119-125 (2021).
964   29.   Siddiqui, I.*, et al.* Intratumoral Tcf1(+)PD-1(+)CD8(+) T Cells with Stem-like Properties Promote
965   Tumor Control in Response to Vaccination and Checkpoint Blockade Immunotherapy. *Immunity*
966   **50**, 195-211 e110 (2019).
967   30.   Miller, B.C.*, et al.* Subsets of exhausted CD8(+) T cells differentially mediate tumor control and
968   respond to checkpoint blockade. *Nat Immunol* **20**, 326-336 (2019).
969   31.   Dammeijer, F.*, et al.* The PD-1/PD-L1-Checkpoint Restrains T cell Immunity in Tumor-Draining
970   Lymph Nodes. *Cancer Cell* **38**, 685-700 e688 (2020).
971   32.   Schoenfeld, A.J. & Hellmann, M.D. Acquired Resistance to Immune Checkpoint Inhibitors.
972   *Cancer Cell* **37**, 443-455 (2020).
973   33.   Travis, W.D.*, et al.* IASLC Multidisciplinary Recommendations for Pathologic Assessment of Lung
974   Cancer Resection Specimens After Neoadjuvant Therapy. *J Thorac Oncol* **15**, 709-740 (2020).
975   34.   Kim, N.*, et al.* Single-cell RNA sequencing demonstrates the molecular and cellular
976   reprogramming of metastatic lung adenocarcinoma. *Nat Commun* **11**, 2285 (2020).
977   35.   Cao, J.*, et al.* The single-cell transcriptional landscape of mammalian organogenesis. *Nature* **566**,
978   496-502 (2019).
979